Magma decompression rate calculations with EMBER: A user-friendly software to model diffusion of H_2O, CO_2 and S in melt embayments

Guillaume Georgeais[1], Kenneth T. Koga[1],Yves Moussallam[2,3], Estelle F. Rose-Koga[1]

[1]*Université Clermont Auvergne, CNRS, IRD, OPGC, Laboratoire Magmas et Volcans, F-63000 Clermont-Ferrand, France*

[2]*Lamont-Doherty Earth Observatory, Columbia University, New York, NY 10027, USA*

[3] *Department of Earth and Planetary Sciences, American Museum of Natural History, New York, NY 10024, USA*

Corresponding author: Guillaume Georgeais; guillaume.georgeais@uca.fr

Keywords: volcanic eruption, magma degassing, conduit processes, volatile element exsolution, GUI

Highlights:

- EMBER is a new, freely available, GUI software that models magma ascent rates for basalt to rhyolite with H2O, CO2 and S diffusion profiles
- EMBER was validated by reproducing previous published literature data
- For mafic eruptions, we found a notable correlation between maximum recalculated decompression rates and eruption magnitude or plume height

ABSTRACT

Magma decompression rate is one of the most important parameters in controlling eruption dynamics. One way to determine decompression rate is by fitting a volatile elements diffusion profile to a concentration gradient in crystal-hosted embayments. Previous studies have used a variety of diffusion models, limiting the possibility for inter-study comparison. Here, we introduce EMBER (EMBayment-Estimated Rates), a standalone versatile tool that models diffusion of volatile elements along melt embayments. Our model relies on the *pdepe* function of MATLAB to calculate diffusion profiles of H_2O, CO_2 and S through the finite difference method. EMBER uses a grid search seeking out the best fits for decompression rates, initial dissolved concentration of each studied volatile and initial exsolved gas content, while setting three constants: temperature along the ascent and pressure at the beginning and end of the ascent. Our model can compute the rate for basaltic, intermediate, and rhyolitic compositions. We applied EMBER to previous studies to evaluate and validate our model. We then re-processed ”homogeneously” the raw data from the literature for a comparison. In other words, the same protocol was used for each diffusion profiles removing the literature-specific strategies used to constrain unknown parameters. With this comparison, we found a statistically significant positive correlation between maximum magma decompression rates and explosivity of the related eruption. EMBER is expected to help increase the number of volatile diffusion in embayments studies aiming at constraining magma decompression and ascent rates and to facilitate inter-study comparisons.

1. INTRODUCTION

Magma ascent rate is a fundamental physical parameter in determining the behavior of a volcanic eruption. Magma ascent rate can be estimated in several ways, during ascent and eruption by geophysical methods, or after the eruption using geochemical and petrological methods. One example of a geophysical method is the analysis of volcanic earthquakes, in which the progressive migration of tremors from a depth to the surface is interpreted as the upward migration of ascending magma [e.g., Aki and Koyanagi., 1981; Scandone and Malone., 1985; Klein et al., 1987; Tryggvason., 1994]. Geochemical methods to determine magma ascent rate are numerous but most of them are only applicable to limited melt compositions. In andesitic magma for instance, the thickness of amphibole breakdown rims has been used to determine ascent rates based on the experimentally-determined rate of the break-down reaction [e.g., Carey and Sigurdsson., 1985; Rutherford and Hill., 1993; Geschwind and Rutherford., 1995; Browne and Gardner., 2006]. Another example is the use of diffusion profiles (e.g., Fe-Mg or H_2O) at the rims of minerals in mantle xenoliths as they re-equilibrate with their carrier melt on their way to the surface [e.g., Mackwell and Kohlstedt., 1990; Klügel et al., 1997; Klügel., 1998; Kohlstedt and Mackwell., 1998; Le Voyer et al., 2014]. Knowing the diffusion coefficient of the species of interest, one can derive an estimate of the magma ascent rate for these eruptions [e.g., Demouchy and Mackwell., 2006; Sparks et al., 2006; Rutherford., 2008]. Another method, based on nucleation theory, links the bubble number density in erupted products (measurable from 2D and 3D observations) to the magma decompression rate [Toramaru., 1989, 1995, 2006]. This theoretical relationship has been reproduced experimentally but is not applicable to natural samples, once bubbles start to coalesce [e.g., Martel and Iacono-Marziano., 2015].

One method, which holds the potential to be widely applicable for a wide range of magma compositions and decompression rates, is the analysis of the diffusion profiles of

volatile elements along melt embayments (also called re-entrants). Embayments are crystal-hosted elongated melt pockets of various shapes and sizes, opened to the outside melt [e.g., Anderson., 1991]. Their formation mechanism is similar to that of melt inclusions [e.g., Faure and Schiano., 2005], through either crystallization around a defect or dissolution of the host crystal, with the exception that they remain connected to the surrounding bubbly melt. They have been studied in quartz [e.g., Liu et al., 2007; Myers et al., 2018], in plagioclases [e.g., Humphreys et al., 2008] and olivine crystals [e.g.,Lloyd et al., 2014; Ferguson et al., 2016; Moussallam et al., 2019], in quenched material ranging from basalt to rhyolite in composition. During magma ascent, the volatile content of the melt surrounding the embayment will decrease, maintaining equilibrium with the exsolved gas phase. The limited volume of melt embayments, however, often prevents bubble formation inside, resulting in embayment melt being super-saturated in volatiles compared to the surrounding melt. This difference in chemical potential leads to a concentration gradient and to diffusive transport of volatile species from the interior to the mouth of the embayment resulting in a diffusion profile. If such a profile is preserved in natural samples, it can then be inverted to derive a decompression rate assuming that the elongated tubular shape of the embayment and the relative impermeability of the host crystal led to unidirectional (1D) diffusion and prevented any advective melt motion in the embayment. The dependency of volatile diffusion in embayments on multiple parameters (melt composition, temperature, pressure, degassing path, decompression rate) makes the interpretation of natural diffusion profiles a challenging endeavour. A numerical model adapted to a wide range of magma compositions is therefore needed to generate multiple diffusion profiles with known parameters and find the synthetic profile which most closely reproduces the measurement.

1.1 Existing embayment volatile diffusion models

Several such numerical models have been developed in the last decades (Table 1). The first published code was developed in FORTRAN 77 [Liu et al., 2007]. Assuming a certain temperature, pressure, initial concentration, exsolved gas, degassing path and decompression rate, the code generated time-dependent profiles of H_2O and CO_2 concentrations until the fragmentation pressure is reached. The process was repeated several times with different decompression rates to find the best fit. A second model was presented by Humphreys et al., [2008] using the COMSOL multiphysics software to model only H_2O profiles. Their model imposes the final concentration at the mouth of the embayment from the start of the calculation and allows the software to run the diffusion calculation. Lloyd et al., [2014] developed a model calculating simultaneously, for a range of decompression rates, three volatile element profiles at once: H_2O, CO_2 and S. In a following study, an improved development of a MATLAB code by Ferguson et al., [2016] took H_2O, CO_2 and S into account and considered not only a range of decompression rates but also the initial concentration of each volatile element as well as the exsolved gas content at the beginning of the ascent (M_0) for basaltic compositions. The addition of this new parameter: (M_0), the pre-existing (already exsolved volatile content in equilibrium with magma at the onset of a magma ascent), proved to have a significant impact on the modelled profile and made the grid search more complex and the result better constrained [Ferguson et al., 2016]. Another study subsequently build the FORTRAN 77 model from Liu et al., [2007] in MATLAB with updated diffusion coefficients for rhyolitic compositions and a best fit search algorithm [Myers et al., 2018]. This code was later updated taking the pressure at which degassing stops as a free parameter [Myers et al., 2021]. Another code, written in Rstudio and restricted to basaltic melts, took into account all the aforementioned parameters with fixed inputs and was made openly available [Moussallam et al., 2019]. One of the most recent model is tuned to intermediate magma compositions, contains a specific S solubility relation and a general H_2O

diffusion coefficient relation for intermediate magma, and looks for the decompression rate and initial pressure [Newcombe et al., 2020]. The latest model to date is written in Matlab and uses grid searches to find decompression rate, initial concentration of H_2O and S and exsolved gas content [Moussallam et al., 2021].

At present, seven different data processing methods to model volatile diffusion profiles in embayments exist; each published study uses its specific model written on four different platforms (FORTRAN 77, COMSOL, MATLAB and RStudio). Other than the code of Moussallam et al., [2019], none are directly downloadable without a specific request to the authors. Each code considers different input parameters, different volatile species and is tuned to a specific melt composition. This lack of consistency is an issue for inter-study comparison and the lack of open software access can be an impediment to a large number of new studies on natural products.

The aim of this article is to provide the community with a user-friendly and cross-operating system MATLAB code that is able to constrain decompression rates from volatile diffusion in melt embayments for rhyolitic to basaltic melt compositions, and for as wide a range of starting conditions as possible. We then retroactively analyze all volatile diffusion profiles from the literature using EMBER. Our results help identify potential discrepancies in published decompression rates, notably for the Mt St Helens 1980's eruption, and provide an easily comparable, self-consistent summary of decompression rates obtained from volatile element diffusion in melt embayments published to date. Our software, EMBER, calculates results likely comparable to those by the DIPRA software [Girona and Costa., 2013], which can extract timescales from diffusion zoning in olivine crystals, and is also a widely distributed MATLAB program.

2. Code architecture

2.1 Diffusion model

Volatile element diffusion in embayments can be regarded as a 1D process, because of their elongated, tube-like geometries and the incompatibility of the elements in their mineral host [Ferguson et al., 2016; Humphreys et al., 2008; Liu et al., 2007; Lloyd et al., 2014; Moussallam et al., 2019, 2021; Myers et al., 2018, 2021; Newcombe et al., 2020]. While this is a commonly accepted assumption, further studies are needed to assess the impacts of the three-dimensional shape of embayments to volatiles diffusion [deGraffenried and Shea., 2020]. If it proves to be relevant, EMBER will need to be updated accordingly to compute both 1D and 3D diffusion. The evolution of the concentration gradient is therefore described by Fick's Second Law (Eq.1):

$$\frac{\partial C}{\partial t} = \frac{\partial}{\partial x}\left(D(x,t)\frac{\partial \ C}{\partial x}\right) \quad (1)$$

$$C = C_i \ at \ x > 0, t = 0 \quad (2)$$

$$C = \ C_{sat}(t) \ at \ x = 0, t > 0 \ ; \ \frac{dC}{dx} = 0 \ at \ \ x = X, t > 0 \quad (3)$$

where D is the diffusion coefficient of the studied volatile species; C, the concentration of studied species, x, the distance from the mouth of the embayment, X, the distance at the interior of the embayment, C_{sat}, the saturation concentration calculated at the mouth of the embayment by using a solubility model, C_i, the initial concentration along the embayment and t, the time. These diffusion equations show that diffusion coefficients depend heavily on H_2O concentration(C_{H_2O}), temperature and pressure. These three parameters, and therefore the diffusion coefficient, all change during ascent. Diffusion coefficients are hence calculated along every point of the embayment from the start to the end of the calculation.

166 The boundary condition at the interior is defined by an absence of mass flux (Neumann
167 condition) (Eq.2) and the volatile concentration at the mouth of the embayment is fixed but
168 varies with respect to time t (Dirichlet boundary condition). The initial volatile concentration
169 C_{init} along the embayment is constant, and the value should be the concentrations of volatile
170 elements at the initiation of magma ascent. Volatile concentration at the mouth of the
171 embayment is set by the solubility of each volatile species along a pressure related path of the
172 magma ascent, and these constraints are entered into EMBER as a text file. For example,
173 EMBER's default setup reads output files from SolEx [Witham et al., 2012], and VolatileCalc
174 [Newman and Lowenstern., 2002] depending on magma types.

175 Solubility of gas species depends on T, P, magma composition and exsolved gas content
176 (M_0). EMBER does not calculate the solubility of volatiles and uses an "external" solubility
177 model like VolatileCalc [Newman and Lowenstern., 2002], Solex [Witham et al., 2012] or
178 any other model that the user chooses to calculate the degassing paths. Since the value of M_0
179 is initially unknown, a typical calculation is done by choosing a "target exsolved gas content"
180 thus by setting a corresponding degassing path. EMBER works with seven solubility files
181 accounting for M_0 values of 0, 0.1, 0.2, 0.4, 0.8, 1.6, 3.2 wt. %, which are supplied by the
182 user. EMBER interpolates those seven degassing paths to find the degassing path associated
183 with the targeted exsolved gas content. It should be noted that, when VolatileCalc-generated
184 degassing paths are used, EMBER imposes the reference point concentrations of 0.01wt. %
185 H_2O, 1 ppm CO_2 and 1 ppm S at P=1 bar because VolatileCalc does not model the degassing
186 path down to one bar.

187 EMBER calculates all model diffusion profiles of the volatile elements following the
188 grid search which range is defined by the user, before iteratively comparing measured and
189 calculated profiles. First, profiles are calculated by varying three parameters for each
190 calculation loop: constant decompression rate, initial volatile content and exsolved gas

content, for each element. Parameters such as temperature, melt composition, initial pressure prior to ascent and pressure at which decompression stops are specified together with the volatile species of interest (H_2O, CO_2, S) and they are fixed for all calculations. The program calculates diffusion profiles using finite difference formulation solved with the *pdepe* function, an ordinary differential equation (ODE) solver from MATLAB.

Diffusion coefficients used in the model calculations are based on the following equations and calculated for each step of the ascent and at each point of a given profile. Water diffusion coefficient (D_{H_2O}) in $m^2.s^{-1}$ for basaltic melt is given by

$$D_{H_2O} = \exp\left[-11.924 - 1.003\ln\left(C_{H_2O}\right)\right] * \exp\left[\frac{-\exp\left(11.836-0.139\ln\left(C_{H_2O}\right)\right)}{RT}\right] \quad (4)$$

where C_{H_2O} is water concentration in wt. %; R, the gas constant in $J.mol^{-1}.K^{-1}$ and T, the temperature in Kelvin [Freda et al., 2003]. For melt with intermediate composition ($55 < SiO_2 < 70$ wt. %), the water diffusion coefficient ($D_{H_2O_t}$ in $m^2.s^{-1}$) is calculated using a combination of equations (5a-i), from Ni and Zhang., [2018], as previously used by Newcombe et al., [2020]:

$$D_{H_2O_t} = D_{H_2O_m}\left(1 - \frac{dX_{OH}}{2dX}\right) + D_{OH}\frac{dX_{OH}}{2dX}, \quad (5a)$$

$$D_{H_2O_m} = D_0\exp(aX), \quad (5b)$$

$$D_{OH} = const, \quad (5c)$$

$$\frac{dX_{OH}}{2dX} = \frac{1-2X}{\sqrt{4X(X-1)\left(1-\frac{4}{K}\right)+1}}, \quad (5d)$$

$$lnK = 2.6Y_{SI} - \frac{4339Y_{SI}}{T}, \quad (5e)$$

$$a = -94.07 + 74.112Y_{SI} + \frac{198508-166674Y_{SI}}{T}, \quad (5f)$$

$$lnD_{OH} = -16.78 - 37.428Y_{SI} - \frac{39250-27576Y_{SI}}{T}, \quad (5g)$$

$$\ln\left(\frac{D_{OH}}{D_0}\right) = -56.09 - 115.93Y_{SI} + 160.54\sqrt{Y_{SI}} - \frac{3970\sqrt{Y_{SI}}}{T}, \quad (5h)$$

$$lnD_0 = 8.02 - 31Y_{SI} + 2.348PY_{SI} + \frac{121824Y_{SI}-118323\sqrt{Y_{SI}}-(10016Y_{SI}-3648)P}{T}, \quad (5i)$$

with Y_{SI}, the mole fraction of Si among all cations, D_0,a diffusion parameter in $m^2.s^{-1}$, K, the equilibrium constant, X, the mole fraction of each species, P in GPa, T in Kelvin, a, a dimensionless parameter, D_{OH} the OH diffusivity in $m^2.s^{-1}$, $D_{H_2O_m}$, the molecular H_2O diffusivity in $m^2.s^{-1}$ and $D_{H_2O_t}$, the total H_2O diffusivity in $m^2.s^{-1}$.

For rhyolitic melt, the water diffusion coefficient (in $\mu m^2.s^{-1}$) is given by,

$$D_{H_2O} = C_{H_2O}\exp(10.49 - \frac{10.661}{T} - \frac{1.772P_t}{T}) \quad (6a)$$

for low (≤ 2 wt. %) water melt, where P_t is the pressure in MPa at time t [Zhang and Behrens., 2000]. However, if the water content is high (from 2 to 8 wt. %), diffusion coefficient is calculated by,

$$D_{H_2O} = X\exp(m)\left\{1 + \exp\left[56 + m + \mathrm{X}\left(-34.1 + \frac{44620}{\mathrm{T}} + \frac{57.3\mathrm{P_t}}{\mathrm{T}}\right) - \sqrt{\mathrm{X}}\left(0.091 + \frac{4.77*10^6}{\mathrm{T^2}}\right)\right]\right\} \quad (6b)$$

where $m = -20.79 - 5030/T - 1.4\,P_t/T$, and X = $\left(C_{H_2O}/18.015\right)/\left[C_{H_2O}/18.015 + \left(100 - C_{H_2O}\right)/32.49\right]$ [Zhang and Behrens., 2000]. The diffusion coefficient of CO_2 (D_{CO_2}), in $m^2.s^{-1}$, is given by,

$$D_{CO_2} = \exp\left[-14.34 - \frac{17360-0.6527P_t}{T} + \left(-0.7171 + \frac{1436.8}{T}\right)C_{H_2O}\right] \quad (7)$$

for basalts to rhyolites [Nowak et al., 2004; Zhang et al., 2007]. The program also calculates diffusion coefficient of S (D_S), in $m^2.s^{-1}$:

$$D_S(i) = \exp\left(-8.21 - \frac{27692-651.6\,C_{H_2O}}{T}\right) \quad (8)$$

[Zhang et al., 2007]. It is to be noted that the sulfur diffusivity determined by Zhang et al., [2007] is applicable only to basaltic melts under reduced conditions [Zhang et al., 2007].

2.2 Best fit determination

The second part of the code compares a measured concentration profile to a series of calculated ones (with N set of parameters) to find the best fit and its associated parameters (i.e. grid search). EMBER favours the grid search over other more efficient optimization methods (*e.g.* gradient search method), because with the mixture of diffusion of dissimilar species, it is not clear *a priori* if there will always exist a unique solution. While computationally intensive (and inefficient), we consider it is more suitable to take an approach of "calculate-all". The best fit is determined by comparing the dimensionless normalized residual square error ($NErr_j$) for each j of N sets of parameters,

$$NErr_j = \sum_i \frac{1}{u_j{}^2}(C_{ij} - Cs_{ij})^2 \quad (9)$$

where u_j is the analytical measurement uncertainty applied at the highest volatile concentration measured in the embayment; usually at the interior of the embayment (*i.e*: an uncertainty of 5% of Cs_{ij}_max), i denotes discrete points along the distance to the embayment mouth, C_{ij} is the calculated concentration and Cs_{ij} is the measured concentration. Among the generated profiles, the one that gives the minimum $NErr_j$ is the best fit. One may calculate $NErr_j$ by considering the "weighting and scaling of the error" of each volatile (further details can be found in part 4.5). By doing so, the program first calculates $NErr_j$ values without

dimensions thanks to u_j. The term u_j effectively constrains the "weight" of three diffusion profiles (H_2O, CO_2, and S) as measurements with better uncertainty (in relative term) have a stronger influence to the sum total of three $NErr$. EMBER then scales the $NErr$ values between each volatiles before adding them. If one chooses not to weight and scale each volatile species' error, $u_j = 1$.

EMBER assesses statistical variations of $NErr$ by a Monte Carlo simulation accounting for the uncertainty of the measurement C ± σ, using a Gaussian distribution random function to generate m iterations of possible profiles within measurement uncertainties. Therefore, for a parameter set (*i.e.* case j), there is m number of $NErr$ computed by comparing a calculated profile against m numbers of the randomly generated profiles $Cs_i + \varepsilon$ (Figure 1, Step 1). A similar approach is taken for the uncertainty of x. The result of this simulation is represented by a mean ($Nerr\_m$) and its related 1-σ confidence interval for a parameter set j (Figure 1, Step 2).

2.3 Propagation of errors

The uncertainties on the fit parameters $Ci,\ dPdt\ and\ M_0$ $(to\ a\ lesser\ extent)$ are assessed by the statistical distributions of the parameters that are extracted from the calculated profiles y that satisfy the following condition (Figure 1. Step 3):

$$\Pr(a - \sigma_1 \leq y \leq a + \sigma_2) = 68\% \quad (10)$$

Here, a is the value for which $Nerr\_m$ is the smallest, and $\sigma_1\ and\ \sigma_2$ respectively the lower and upper boundaries of the confidence interval, calculated using the *prctile* MATLAB function. For every j calculated profiles (with a set of parameters), there is a corresponding $NErr$. Equation (10) states that there are cases of calculated profiles for which $NErr$ is within the expected uncertainty. EMBER extracts the corresponding parameters (dPdt and C_i) and

report the distribution of values as mean and 1-σ confidence interval, which are the best fit parameter and an associated uncertainty (Figure 1. Step 4 and 5). In consequence, measurement uncertainties must be entered by the user in EMBER because of the Monte Carlo error propagation. An uncertainty on the distance between two measurement spots is set by default at ±2 µm and can be changed to whichever value the user requires, down to 0 µm if needed.

3. Examples of model outputs

3.1 Organization of the graphical user interface

EMBER runs inside a user-friendly Graphical User Interface (GUI) upon execution of the application file. The GUI is separated in two parts: the input section, dedicated to generating the grid search and decompression conditions (left hand side Part1, panels a, b, c; Fig.2), and the results section dedicated to displaying the results once calculation is terminated (Part 2, panels a, b; Fig. 2). Panel 2c display a process log during the calculations. Figure 3 shows the result of a simulation using the volatile profiles measured in an embayment from the study of Ferguson et al., [2016] as an example. Unticking the "Weighting and scaling of error" checkbox will remove the scaling of NErr. The u_j parameter from equation (8) is set to 1 in this case and NErr is not scaled before being added for the cumulative error calculation. In such case, as all concentration are treated as weight percent internally, the H_2O profile will usually weight more than the others as it usually records much larger variations in absolute concentration.

3.2 Outputs of the calculation

Figures generated by EMBER have two purposes: (1) to display the results of the calculation and (2) to track the variation of the best-fit estimation with parameters from the grid search such as M_0 or C_i. Figure 3a shows the influence of the exsolved gas content to the resulting best-fit diffusion profile. Other parameters can be tested. For example, the number of volatile species fitted at once (single or up to 3, solid line or dashed line, respectively; Fig. 3b) also influences the resulting best-fit profile. Figure 3c shows the sensitivity of the cumulative error over decompression rate and exsolved gas content (M_0). Figure 3d shows the influence of the initial concentration on each volatile best fit error calculation.

Each figure generated is saved in a unique file (.fig) directly openable with EMBER. Along with the figures, EMBER also produces four Excel (.xls) files (.csv for Mac). They contain the input parameters, the diffusion profiles of each best case, for every decompression rate with the best C_i and M_0, and a copy of the results for each volatile with the respective exsolved gas content.

4. Calculation and performance test

4.1 A priori requirements

As with all computational software, meaningful results in EMBER will only be achieved with appropriate dataset. Investigations should be limited to entirely glassy embayments, sampled from rapidly quenched deposits (e.g., <2 cm sized tephra), exhibiting a geometry that is close to that of a cylinder with constant radius. More complex geometries would void the core assumption of unidirectional diffusion and necessitate 3D diffusion modeling. [e.g., deGraffenried and Shea., 2020], which is not currently supported by EMBER. The longer the embayment, the more likely it is to display a concentration plateau in the diffusion profile indicative of C_i and the starting pressure of ascent (P_{Start}). In absence of such condition, we recommend the user to determine P_{Start}, C_i and T from melt inclusions and geo-

thermobarometry studies. Finally, volatile concentration measurements on surrounding glass are required to assess P_{end}, the pressure of quenching.

While we used VolatileCalc and SolEx as the main degassing path generators in the examples below, it should be noted that EMBER can also read degassing paths from any other software as long as the input files comply with the required format (see the tutorial in the additional instructions). Hence, the choice of degassing path software is ultimately up to the user's preference.

4.2 Comparison with previous studies

We re-analysed the natural volatile diffusion profiles in embayments from previous studies, to assess the quality of EMBER's decompression rate calculation: from the 1980 Mt St Helens [Humphreys et al., 2008], 1974 Fuego [Lloyd et al., 2014], 1500, 1650 and 1959 Kīlauea [Ferguson et al., 2016], 27 ka Taupo [Myers et al., 2018], 767 ka Long Valley [Myers et al., 2018], 2 Ma Yellowstone [Myers et al., 2018], 2017-2018 Ambae/Aoba [Moussallam et al., 2019], Late Bronze Age (LBA) Santorini [Myers et al., 2021] and December 2018 Ambrym [Moussallam et al., 2021] eruptions. We used the uncertainties reported in each study when provided. Also when provided, we directly used the specific grid search (e.g. Ferguson et al., [2016] provides a range of M_0). Otherwise, we estimated the possible range of grid search from the reported uncertainties for decompression rates and initial concentrations. Degassing paths were calculated respecting P, T, and volatile contents used in the original studies (typically, we use SolEx or VolatileCalc when authors specified it). Similarly, the re-analysed results were calculated using the same set of values for M_0 as the original literature data to which they are compared. In detail this was M_0 = 0.1, 1.6, 1.6, 0.8 wt. % respectively for IkiE1, ReticE1, ReticE2 and KeaE1 [Ferguson et al., 2016], M_0 = 0.4, 0, 0, 3.2 wt. % respectively for AF2, AD5, AE38 and PG11 [Moussallam et al., 2021] and M_0 = 0 wt. % for

all embayments from Ambae [Moussallam et al., 2019]. For all other studies of which the exsolved gas content was not specified we used M_0 = 0 wt. %. In some cases [Myers et al., 2018], we limited our tests to three samples from each investigated eruption, making sure to test the samples with the highest and lowest estimation. All results except those from Ambrym were calculated with the weighting and scaling of the error. The results are shown in Figure 4.

There is a good agreement between EMBER results and most literature values. Data from the 1980's Mt St Helens eruption [Humphreys et al., 2008] show consistent disparity between the published decompression rates and EMBER's. This difference is due to significantly different boundary conditions of this study compared with the original. The model from the original study [Humphreys et al., 2008] fixed the final concentration at the mouth of the embayment, prior to the ascension. Since the diffusion phenomenon is gradient-dependent, imposing a high concentration gradient at the beginning of the simulation should lead to faster volatile diffusion and a higher decompression rate estimation. This is a critical simplification leading to significant differences in the calculated decompression rate. Other minor differences observed between our re-analysis and earlier decompression rates estimates come from (1) the use of a different H_2O diffusion coefficient as well as a single episode of ascent in all our calculation (as opposed to two-step ascent; [Lloyd et al., 2014]), (2) the calculation of diffusion coefficient (e.g., taking into account the change of diffusivity due to H_2O diffusion or choosing different equations of diffusivity) and (3) the weighting and scaling of error associated with each volatile diffusion profile in all our calculations (Fig.4).

4.3 Monte Carlo simulation

We ran tests on three samples with variable number of Monte Carlo iterations (m=3, 11, 101, 501 and 1001) to determine the lowest number of the iterations to achieve stable assessment

of uncertainties: BT251, a rhyolite from Long Valley, ReE2, a reticulite from 1500 CE Kīlauea lava fountain and AO02, a basalt from phase 2 of the 2017-2018 eruption of Ambae. For BT251, the representation gradually acquires the shape of a pseudo-gaussian distribution with increasing iteration counts. The median and mean values of all filtered decompression rate do not change significantly with increasing iterations (Fig 5) and a stability of the data distribution is quickly achieved (for m=11). For ReE1, the precision of the nanoSIMS measurements and the low decompression rate leads to a stable calculation and a needle shaped histogram even for m=3, suggesting that the results are well constrained. For AO02 the shape of the histogram is pointy, unimodal and skewing right with a long tail. With higher dP/dt values (i.e., sharper diffusion profiles), modelled diffusion profiles become more and more similar, making it harder for the software to find the best solution. This results in a skewed solution histogram with a long tail and a more noticeable difference between mean and median value. For such cases, stability is reached for m = 101. We recommend 101 iterations (EMBER default iteration value) as it was enough to reach a stable solution for our most uncertain case.

4.4 How well does EMBER constrain M_0?

Calculation of the exsolved gas content has been introduced within the embayment method with the calculations made by Ferguson et al., [2016]. They noted it had a significant influence on their calculation of decompression rate, which was confirmed by later studies and by EMBER (Fig 3a and Fig 6a). The effect is mostly a result of the exsolved gas content having a large influence on the degassing trend. From our investigation of literature data, we see that a change of M_0 from 0 to 3.2 wt. % can cause the decompression rate estimation to increase by 10 fold (Fig 6 (a)). This variation is most pronounced on H_2O profiles in embayments of basaltic composition (Fig 6 (a), (b), (c)). Except for these few cases, the

impact of M_0 is hardly significant enough for it to be accurately determined using only diffusion profiles (the associated error frequently covering the entire range studied).

The change of decompression rate in response to variable M_0 illustrates the importance of P_{end} (Fig. 6 (d)) (which must be determined from measured data) and the critical influence of the modelled degassing path.

The best fit M_0 values are directly affected by the choice of P_{end} (Fig. 6 (d)) which must be determined from measured data. Taking as an example, the calculation of one profile from Ferguson et al., [2016] which ends at a specified quenching pressure P_{end} = 2.75 MPa. Using the decompression path (from SolEx) for M_0<1.6 wt. %, the resulting H_2O concentration at P=2.75 MPa would be higher than C_S(x = 0), the measured concentration at the mouth of the embayment approximated with the glass measurement, by up to 0.20 wt. %. Synthesized diffusion profiles in this case cannot reproduce the concentration at the mouth of the embayment for M_0<1.6 wt. %. Because of this limitation, as shown in figure 3a, only a degassing paths associated with at the best fit M_0 value could match the whole diffusion profile by fitting the concentration at the mouth. It should be noted that if a different Pend is chosen, it is possible that EMBER finds another best-fit M_0 (Fig 6 (d)). Therefore, we advise the user to be cautious when choosing Pend for decompression rate modelling, especially in case constrained by one volatile species (Fig 6 (e), (f)).

4.5 Weighting and scaling of error

EMBER leaves the user the choice to, or not to, equally weigh and scale the relative contribution of each volatile profile equally, when calculating the cumulative error. For example, the study from Ferguson et al., [2016] gives equal weight ($u_j = 1$) to all three volatile species, except on a few cases. By doing so, the best fit $NErr_j$ calculated from H_2O

profiles is several orders of magnitude higher than the best fit $NErr_j$ calculated for CO_2 or S profiles. That difference is due to the range of concentration variation, as H_2O usually varies within a few wt. % and CO_2 and S usually varies within thousands of ppm at best. Cumulative error calculation, and subsequently the best fit determination, becomes heavily dependent on the H_2O $NErr_j$ value, making the constrains brought by CO_2 or S profiles almost negligible. Another approach is to weight the $NErr_j$ values either with analytical uncertainty [Myers et al., 2018] or maximum measured concentration in the embayment [Newcombe et al., 2020] of volatile species. Weighting the concentration with the error value nondimensionalizes the profile and gives equal weight to the quality of fit of each volatile specie. In EMBER, the $NErr_j$ values are weighted by the analytical uncertainty on each volatile concentration. It results in an even consideration of the constraints brought by each volatile species. There are pros and cons for this choice, if one thinks the S degassing model to not be as accurate as the H_2O degassing model for instance, one may choose not to weigh and scale the errors. The user ultimately must make the choice and it should be reported.

5. Recalculation of decompression rates

In the previous section, we presented EMBER calculation results using initial conditions (C_i, M_0 if studied, range of dPdt, P_{end}, P_{start}) directly from the original literature studies to demonstrate the quality of EMBER and its ability to reproduce the former literature results. Now, we use EMBER to reprocess the raw data from the literatures, but this time using a uniform protocol that takes into account the following parameters: the presence of exsolved gas, the same set of formulas for diffusion coefficient calculation, a model with a single step ascent and an initial volatile element concentration, determined from the concentration plateau (Table 2). Detailed modelled profiles of each embayments can be found in the supplementary materials. We restricted the calculations to 3 profiles per eruption for Myers et

al., [2018], including the ones associated with the highest and lowest decompression rate recorded, and to 5 profiles for Myers et al., [2021].

5.1 The impact of calculation strategies

Our hope with developing EMBER is to minimize differences in modelling parameters (e.g., diffusion coefficients, error treatment, minimization strategy…) in future studies. It is important to realize however that differences in strategies will persist. For instance, whilst EMBER allow the user to set the exsolved gas content (M_0) as a free parameter to be determined by a grid-search, some users might prefer to impose an exsolved gas content based on independent constraint. This is the case for instance of the Moussallam et al., [2019] study of the 2017-2018 Ambae eruption where, in a second set of calculations, the authors used the difference between the volatile content of the melt inclusions and the starting volatile content of the embayments to estimate the likely amount of exsolved volatile in the system at the initiation of ascent.

Another strategy is to use the volatile content of melt inclusions as starting conditions for the diffusion model instead of the measured plateau values in the embayment interior. This was the strategy adopted by Myers et al., [2021] for the Minoan eruption of Santorini, were a fixed initial concentration of 5.2 wt. % H_2O (except for one embayment at 5.6 wt. % H_2O) was used for all model calculations. Such strategy was also used by Humphreys et al., [2008] for Mt St Helens calculations.

In this study, we recalculated all embayment profiles using the same strategy throughout, but we do not pass judgement on the validity of one strategy over another. Our aim is to present a dataset which is as comparable as possible. The data presented in Fig. 7 and Table 2 are hence all calculated leaving the exsolved volatile content (M_0) as unconstrained (i.e., as a part of the

grid search) and using the plateau values in volatile content recorded in embayment interiors as the model starting conditions (C_i).

This difference in starting assumptions can lead to significant differences in the resulting decompression rate. Recalculating the embayment data from Myers et al., [2021] with our protocol leads to decompression rates 3 to 20 times higher. It is therefore of paramount importance that users of EMBER explicitly report their assumptions and starting conditions. We recommend that future compilations continue to reprocess original data in a consistent manner (as done here) in order to render inter-study comparison as coherent as possible.

5.2 Decompression rates vs eruption parameters

A recent literature compilation showed a clear relationship between magma decompression rate and whether an eruption is explosive or effusive in character [Cassidy et al., 2018]. This relationship deserves more scrutiny to establish if finer relationships between magma decompression rates and explosivity exists in nature. The VEI (Volcanic Explosivity Index), as an approximation of eruption explosivity, is related to eruption magnitude and/or plume height [Newhall and Self., 1982]. To show the utility of EMBER for the studies of volcanic explosivity, we tested the presence (or absence) of a correlation between decompression rate and both eruption magnitude and plume height, with our reprocessed data. Previous studies have found that the eruption magnitude is positively correlated with decompression rate [Ferguson et al., 2016; Moussallam et al., 2019]. However, our compilation shows no clear correlation between decompression rate and eruption magnitude (Fig. 7a).

We notice that an increase in decompression rate with eruption magnitude is noticeable for basaltic magmas (Kīlauea, Ambae and Ambrym) but the correlation is weakly significant (Pearson coefficient of 0.24 with a p-value of 0.35 and R^2=0.47, which corresponds to a weak

positive correlation). In a single eruption, there can be varying flow regime creating a range of decompression rate within the conduit; a batch of magma potentially ascend faster than the others (e.g., [Martel et al., 1998; Gonnermann and Manga., 2007; Cassidy et al., 2015]). If we only consider the highest decompression rate of any given eruption however, the aforementioned weak correlation between decompression rate and magnitude becomes more significant for mafic eruptions (Figure 7a) (Pearson coefficient of 0.93 with a p-value of 0.01 and R^2=0.86). The calculated decompression rates for rhyolitic eruptions on the other hand shows no correlation with eruption magnitude.

The eruption intensity is also assessed with the plume height, which is directly observed or calculated through several empirically-determined relations involving isopachs for explosive eruptions (e.g., [Woods and Wohletz., 1991; Mastin et al., 2009; Pyle., 2015]). The eruption intensity, estimated from the mass eruption rate, has been shown to be positively correlated with decompression rate [Barth et al., 2019; Ferguson et al., 2016; Newcombe et al., 2020]. Thus, the plume height is expected to correlate with the decompression rate. We used EMBER-recalculated decompression rates to test this hypothesis. For the two eruptions of Kīlauea for which the plume height is not constrained, we used the maximal height of the lava fountain instead. Ambrym's plume height data for the 2018 eruption is undetermined and therefore not added to Figure 7b. Results show no global correlation between these two parameters (Figure 7b). However, considering again the highest decompression rate recorded for each eruption, a strong positive correlation emerges for basaltic eruptions (with a Person coefficient of 0.76, a p-value of 0.005 and R^2=0.88). Again, the calculated decompression rate for rhyolitic eruptions shows no correlation with eruption plume height. The maximum decompression rate for basaltic eruption therefore shows a statistically significant positive correlation with both eruption magnitude and plume height. A first order positive correlation

518 therefore exists between the maximal magma decompression rate and the explosivity of an
519 eruption for basaltic eruptions.

520

521

522 ## 6. Conclusion

523 • We present EMBER, a user-friendly GUI program that calculates decompression rates
524 from H_2O, CO_2 and S concentration profiles along embayments of basaltic to rhyolitic
525 compositions.

526 • We found that decompression rate calculations are particularly sensitive to variations
527 of M_0 especially for the H_2O diffusion profile. Variations of P_{end} are also accompanied
528 by a variation of the best fit exsolved gas content, but not necessarily by a variation of
529 associated decompression rate.

530 • We recalculated decompression rates from previous studies twice: first, to validate and
531 test how well EMBER reproduced existing results using the parameters from the
532 original studies, and secondly, to homogenize determined decompression rates
533 applying the same protocol to the existing raw data from previous studies, in order to
534 improve inter-study comparison.

535 • In the first case, recalculated decompression rates are in the same order of magnitude
536 as original calculations but notable differences do occur such as for the 1980 Mt St
537 Helens eruption which recalculated decompression rate are at 0.15-0.41 MPa/s, half of
538 the previously reported values [Humphreys et al., 2008].

539 • In the second case, recalculated dataset shows no significant correlation between
540 magma decompression rate and eruption magnitude when considering the entire
541 dataset and shows a weak correlation when considering the subset of decompression
542 rates of basaltic magma (Pearson coefficient of 0.24 with a p-value of 0.35 and

543 R^2=0.47.) The correlation is significant when considering only the maximum
544 decompression rates of each basaltic eruption (Pearson coefficient of 0.93 with a p-
545 value of 0.01 and R^2=0.86). Additionally, there is no significant correlation between
546 decompression rate and plume height when considering the entire dataset. However,
547 once again, a statistically significant trend appears when considering only the
548 maximum decompression rate of the basaltic eruptions (with a Person coefficient of
549 0.84, a p-value of 0.007 and R^2=0.88).

550 • Our results suggest for the first time, a significant positive correlation, between
551 embayment-calculated maximum decompression rate and eruption explosivity
552 parameters such as magnitude and plume height, for basaltic eruptions.

553

7. Computer code availability

- Title of the software: EMBER

- Developers: Guillaume Georgeais, Kenneth T. Koga, Yves Moussallam, Estelle F. Rose-Koga

- Hardware used: EMBER was run on a computer with 4 core (4.5GHz) and 16GB of RAM

- Link to the software, tutorial and test using data from [Ferguson et al., 2016] DOI: 10.6084/m9.figshare.13663811

- Software required: MATLAB Runtime Environment 2019b and up https://www.mathworks.com/products/compiler/matlab-runtime.html

Acknowledgement

We would like to thank M. Humphreys for providing the raw data of the Mt St Helens embayments. GG was supported by a PhD fellowship from the French Government "Ministère de l'Enseignement Supérieur, de la Recherche et de l'Innovation". ERK acknowledges partial funding from Laboratory of Excellence initiative n°ANR-10-LABX-0006, the Région Auvergne and the European Regional Development Funds. Y.M acknowledges funding from INSU and the Région Auvergne Rhone Alpes. This is Laboratory of Excellence ClerVolc contribution number 463. We thank Madison Myers for sharing her code during the review process of our manuscript. We would like to thank Madison Myers and an Anonymous reviewer for their comments on the original manuscript and Marie Edmonds for editorial handling.

Bibliography

Aki, K., & Koyanagi, R. (1981). Deep volcanic tremor and magma ascent mechanism under Kilauea, Hawaii. *Journal of Geophysical Research*, *86*(B8), 7095. https://doi.org/10.1029/JB086iB08p07095

584 Anderson, A. T. (1991). Hourglass inclusions: Theory and application to the Bishop Rhyolitic Tuff.
585 *American Mineralogist*, *76*(3–4), 530–547.
586 Barth, A., Newcombe, M., Plank, T., Gonnermann, H., Hajimirza, S., Soto, G. J., et al. (2019). Magma
587 decompression rate correlates with explosivity at basaltic volcanoes — Constraints from
588 water diffusion in olivine. *Journal of Volcanology and Geothermal Research*, *387*, 106664.
589 https://doi.org/10.1016/j.jvolgeores.2019.106664
590 Behrens, H., & Zhang, Y. (2001). Ar diffusion in hydrous silicic melts: Implications for volatile diffusion
591 mechanisms and fractionation. *Earth and Planetary Science Letters*, *192*, 363–376.
592 https://doi.org/10.1016/S0012-821X(01)00458-7
593 Browne, B., & Gardner, J. (2006). The influence of magma ascent path on the texture, mineralogy,
594 and formation of hornblende reaction rims. *Earth and Planetary Science Letters*, *246*(3–4),
595 161–176. https://doi.org/10.1016/j.epsl.2006.05.006
596 Carey, S., & Sigurdsson, H. (1985). The May 18, 1980 eruption of Mount St. Helens: 2. Modeling of
597 dynamics of the Plinian Phase. *Journal of Geophysical Research: Solid Earth*, *90*(B4), 2948–
598 2958. https://doi.org/10.1029/JB090iB04p02948
599 Cassidy, M., Cole, Paul. D., Hicks, K. E., Varley, N. R., Peters, N., & Lerner, A. H. (2015). Rapid and
600 slow: Varying magma ascent rates as a mechanism for Vulcanian explosions. *Earth and*
601 *Planetary Science Letters*, *420*, 73–84. https://doi.org/10.1016/j.epsl.2015.03.025
602 Cassidy, M., Manga, M., Cashman, K., & Bachmann, O. (2018). Controls on explosive-effusive volcanic
603 eruption styles. *Nature Communications*, *9*(1), 2839. https://doi.org/10.1038/s41467-018-
604 05293-3
605 deGraffenried, R., & Shea, T. (2020). Modeling diffusion in 1D within melt embayments: correcting
606 for 3D geometry. Presented at the AGU Fall Meeting 2020, AGU. Retrieved from
607 https://agu.confex.com/agu/fm20/meetingapp.cgi/Paper/676363

608 Demouchy, S., & Mackwell, S. (2006). Mechanisms of hydrogen incorporation and diffusion in iron-
609 bearing olivine. *Physics and Chemistry of Minerals*, *33*(5), 347–355.
610 https://doi.org/10.1007/s00269-006-0081-2
611 Faure, F., & Schiano, P. (2005). Experimental investigation of equilibration conditions during
612 forsterite growth and melt inclusion formation. *Earth and Planetary Science Letters*, *236*(3),
613 882–898. https://doi.org/10.1016/j.epsl.2005.04.050
614 Ferguson, D. J., Gonnermann, H. M., Ruprecht, P., Plank, T., Hauri, E. H., Houghton, B. F., & Swanson,
615 D. A. (2016). Magma decompression rates during explosive eruptions of Kīlauea volcano,
616 Hawaii, recorded by melt embayments. *Bulletin of Volcanology*, *78*(10), 71.
617 https://doi.org/10.1007/s00445-016-1064-x
618 Freda, C., Baker, D. R., Romano, C., & Scarlato, P. (2003). Water diffusion in natural potassic melts.
619 *Geological Society, London, Special Publications*, *213*(1), 53–62.
620 https://doi.org/10.1144/GSL.SP.2003.213.01.04
621 Freda, Carmela, Baker, D. R., & Scarlato, P. (2005). Sulfur diffusion in basaltic melts. *Geochimica et*
622 *Cosmochimica Acta*, *69*(21), 5061–5069. https://doi.org/10.1016/j.gca.2005.02.002
623 Gardner, J. E., Sigurdsson, H., & Carey, S. N. (1991). Eruption dynamics and magma withdrawal during
624 the Plinian Phase of the Bishop Tuff Eruption, Long Valley Caldera. *Journal of Geophysical*
625 *Research*, *96*(B5), 8097. https://doi.org/10.1029/91JB00257
626 Geschwind, C.-H., & Rutherford, M. J. (1995). Crystallization of microlites during magma ascent: the
627 fluid mechanics of 1980–1986 eruptions at Mount St Helens. *Bulletin of Volcanology*, *57*(5),
628 356–370. https://doi.org/10.1007/BF00301293
629 Girona, T., & Costa, F. (2013). DIPRA: A user-friendly program to model multi-element diffusion in
630 olivine with applications to timescales of magmatic processes. *Geochemistry, Geophysics,*
631 *Geosystems*, *14*(2), 422–431. https://doi.org/10.1029/2012GC004427
632 Gonnermann, H. M., & Manga, M. (2007). The Fluid Mechanics Inside a Volcano. *Annual Review of*
633 *Fluid Mechanics*, *39*(1), 321–356. https://doi.org/10.1146/annurev.fluid.39.050905.110207

Humphreys, M. C. S., Menand, T., Blundy, J. D., & Klimm, K. (2008a). Magma ascent rates in explosive eruptions: Constraints from H2O diffusion in melt inclusions. *Earth and Planetary Science Letters*, *270*(1–2), 25–40. https://doi.org/10.1016/j.epsl.2008.02.041

Humphreys, M. C. S., Menand, T., Blundy, J. D., & Klimm, K. (2008b). Magma ascent rates in explosive eruptions: Constraints from H2O diffusion in melt inclusions. *Earth and Planetary Science Letters*, *270*(1–2), 25–40. https://doi.org/10.1016/j.epsl.2008.02.041

Johnston, E., R.S.J., S., Phillips, J., & Carey, S. (2014). Revised Estimates for the Volume of the Late Bronze Age Minoan Eruption, Santorini, Greece. *Journal of the Geological Society*, *171*. https://doi.org/10.1144/jgs2013-113

Klein, F. W., Koyanagi, R. Y., Nakata, J. S., & Tanigawa, W. R. (1987). The seismicity of Kilauea's magma system. *US Geol. Surv. Prof. Pap*, *1350*(2), 1019–1185.

Klügel, A. (1998). Reactions between mantle xenoliths and host magma beneath La Palma (Canary Islands): constraints on magma ascent rates and crustal reservoirs. *Contributions to Mineralogy and Petrology*, *131*(2), 237–257. https://doi.org/10.1007/s004100050391

Klügel, A., Hansteen, T. H., & Schmincke, H.-U. (1997). Rates of magma ascent and depths of magma reservoirs beneath La Palma (Canary Islands). *Terra Nova*, *9*(3), 117–121. https://doi.org/10.1046/j.1365-3121.1997.d01-15.x

Kohlstedt, D. L., & Mackwell, S. J. (1998). Diffusion of hydrogen and intrinsic point defects in olivine. *Zeitschrift Fur Physikalische Chemie*, *207*(1–2), 147–162.

Le Voyer, M., Asimow, P. D., Mosenfelder, J. L., Guan, Y., Wallace, P. J., Schiano, P., et al. (2014). Zonation of H2O and F Concentrations around Melt Inclusions in Olivines. *Journal of Petrology*, *55*(4), 685–707. https://doi.org/10.1093/petrology/egu003

Liu, Y., Anderson, A. T., & Wilson, C. J. N. (2007). Melt pockets in phenocrysts and decompression rates of silicic magmas before fragmentation. *Journal of Geophysical Research*, *112*(B6), B06204. https://doi.org/10.1029/2006JB004500

659 Lloyd, A. S., Ruprecht, P., Hauri, E. H., Rose, W., Gonnermann, H. M., & Plank, T. (2014). NanoSIMS
660 results from olivine-hosted melt embayments: Magma ascent rate during explosive basaltic
661 eruptions. *Journal of Volcanology and Geothermal Research*, *283*, 1–18.
662 https://doi.org/10.1016/j.jvolgeores.2014.06.002
663 Mackwell, S. J., & Kohlstedt, D. L. (1990). Diffusion of hydrogen in olivine: Implications for water in
664 the mantle. *Journal of Geophysical Research*, *95*(B4), 5079.
665 https://doi.org/10.1029/JB095iB04p05079
666 Martel, C., Pichavant, M., Bourdier, J.-L., Traineau, H., Holtz, F., & Scaillet, B. (1998). Magma storage
667 conditions and control of eruption regime in silicic volcanoes: experimental evidence from
668 Mt. Pelée. *Earth and Planetary Science Letters*, *156*(1), 89–99.
669 https://doi.org/10.1016/S0012-821X(98)00003-X
670 Martel, Caroline, & Iacono-Marziano, G. (2015). Timescales of bubble coalescence, outgassing, and
671 foam collapse in decompressed rhyolitic melts. *Earth and Planetary Science Letters*, *412*,
672 173–185. https://doi.org/10.1016/j.epsl.2014.12.010
673 Mason, B. G., Pyle, D. M., & Oppenheimer, C. (2004). The size and frequency of the largest explosive
674 eruptions on Earth. *Bulletin of Volcanology*, *66*(8), 735–748. https://doi.org/10.1007/s00445-
675 004-0355-9
676 Mastin, L., Van Eaton, A., & Lowenstern, J. (2014). Modeling ash fall distribution from a Yellowstone
677 supereruption. *Geochemistry, Geophysics, Geosystems*, *15*.
678 https://doi.org/10.1002/2014GC005469
679 Mastin, L. G., Guffanti, M., Servranckx, R., Webley, P., Barsotti, S., Dean, K., et al. (2009). A
680 multidisciplinary effort to assign realistic source parameters to models of volcanic ash-cloud
681 transport and dispersion during eruptions. *Journal of Volcanology and Geothermal Research*,
682 *186*(1), 10–21. https://doi.org/10.1016/j.jvolgeores.2009.01.008
683 Moussallam, Y., Rose-Koga, E. F., Koga, K. T., Médard, E., Bani, P., Devidal, J.-L., & Tari, D. (2019). Fast
684 ascent rate during the 2017–2018 Plinian eruption of Ambae (Aoba) volcano: a petrological

685 investigation. *Contributions to Mineralogy and Petrology*, *174*(11), 90.
686 https://doi.org/10.1007/s00410-019-1625-z
687 Moussallam, Y., Médard, E., Georgeais, G., Rose-Koga, E. F., Koga, K. T., Pelletier, B., et al. (2021).
688 How to turn off a lava lake? A petrological investigation of the 2018 intra-caldera and
689 submarine eruptions of Ambrym volcano. *Bulletin of Volcanology*.
690 https://doi.org/10.1007/s00445-021-01455-2
691 Myers, M. L., Wallace, P. J., Wilson, C. J. N., Watkins, J. M., & Liu, Y. (2018). Ascent rates of rhyolitic
692 magma at the onset of three caldera-forming eruptions. *American Mineralogist*, *103*(6), 952–
693 965. https://doi.org/10.2138/am-2018-6225
694 Myers, M. L., Druitt, T. H., Schiavi, F., Gurioli, L., & Flaherty, T. (2021). Evolution of magma
695 decompression and discharge during a Plinian event (Late Bronze-Age eruption, Santorini)
696 from multiple eruption-intensity proxies. *Bulletin of Volcanology*, *83*(3), 18.
697 https://doi.org/10.1007/s00445-021-01438-3
698 Newcombe, M. E., Plank, T., Barth, A., Asimow, P. D., & Hauri, E. (2020). Water-in-olivine magma
699 ascent chronometry: Every crystal is a clock. *Journal of Volcanology and Geothermal*
700 *Research*, *398*, 106872. https://doi.org/10.1016/j.jvolgeores.2020.106872
701 Newhall, C. G., & Self, S. (1982). The volcanic explosivity index (VEI) an estimate of explosive
702 magnitude for historical volcanism. *Journal of Geophysical Research*, *87*(C2), 1231.
703 https://doi.org/10.1029/JC087iC02p01231
704 Newman, S., & Lowenstern, J. B. (2002). VolatileCalc: a silicate melt–H2O–CO2 solution model
705 written in Visual Basic for excel. *Computers & Geosciences*, *28*(5), 597–604.
706 https://doi.org/10.1016/S0098-3004(01)00081-4
707 Ni, H., & Zhang, L. (2018). A general model of water diffusivity in calc-alkaline silicate melts and
708 glasses. *Chemical Geology*, *478*, 60–68. https://doi.org/10.1016/j.chemgeo.2017.10.010

709 Nowak, M., & Behrens, H. (1997). An experimental investigation on diffusion of water in
710 haplogranitic melts. *Contributions to Mineralogy and Petrology*, *126*(4), 365–376.
711 https://doi.org/10.1007/s004100050256
712 Nowak, Marcus, Schreen, D., & Spickenbom, K. (2004). Argon and CO2 on the race track in silicate
713 melts: A tool for the development of a CO2 speciation and diffusion model. *Geochimica et*
714 *Cosmochimica Acta*, *68*, 5127–5138. https://doi.org/10.1016/j.gca.2004.06.002
715 Pyle, D. M. (2015). Sizes of Volcanic Eruptions. In *The Encyclopedia of Volcanoes* (pp. 257–264).
716 Elsevier. https://doi.org/10.1016/B978-0-12-385938-9.00013-4
717 Rutherford, M. J. (2008). Magma Ascent Rates. *Reviews in Mineralogy and Geochemistry*, *69*(1), 241–
718 271. https://doi.org/10.2138/rmg.2008.69.7
719 Rutherford, Malcolm J., & Hill, P. M. (1993). Magma ascent rates from amphibole breakdown: An
720 experimental study applied to the 1980–1986 Mount St. Helens eruptions. *Journal of*
721 *Geophysical Research: Solid Earth*, *98*(B11), 19667–19685.
722 https://doi.org/10.1029/93JB01613
723 Scandone, R., & Malone, S. D. (1985). Magma supply, magma discharge and readjustment of the
724 feeding system of mount St. Helens during 1980. *Journal of Volcanology and Geothermal*
725 *Research*, *23*(3–4), 239–262. https://doi.org/10.1016/0377-0273(85)90036-8
726 Self, S. (2006). The effects and consequences of very large explosive volcanic eruptions. *Philosophical*
727 *Transactions of the Royal Society A: Mathematical, Physical and Engineering Sciences*,
728 *364*(1845), 2073–2097. https://doi.org/10.1098/rsta.2006.1814
729 Shreve, T., Grandin, R., Boichu, M., Garaebiti, E., Moussallam, Y., Ballu, V., et al. (2019). From
730 prodigious volcanic degassing to caldera subsidence and quiescence at Ambrym (Vanuatu):
731 the influence of regional tectonics. *Scientific Reports*, *9*(1), 18868.
732 https://doi.org/10.1038/s41598-019-55141-7

Sparks, R. S. J., Baker, L., Brown, R., Field, M., Schumacher, J., Stripp, G., & L. Walters, A. (2006). Dynamical constraints on kimberlite volcanism. *Journal of Volcanology and Geothermal Research*, *155*, 18–48. https://doi.org/10.1016/j.jvolgeores.2006.02.010

Toramaru, A. (2006). BND (bubble number density) decompression rate meter for explosive volcanic eruptions. *Journal of Volcanology and Geothermal Research*, *154*(3–4), 303–316. https://doi.org/10.1016/j.jvolgeores.2006.03.027

Toramaru, Atsushi. (1989). Vesiculation process and bubble size distributions in ascending magmas with constant velocities. *Journal of Geophysical Research*, *94*(B12), 17523. https://doi.org/10.1029/JB094iB12p17523

Toramaru, Atsushi. (1995). Numerical study of nucleation and growth of bubbles in viscous magmas. *Journal of Geophysical Research: Solid Earth*, *100*(B2), 1913–1931. https://doi.org/10.1029/94JB02775

Tryggvason, E. (1994). Surface deformation at the Krafla volcano, North Iceland, 1982–1992. *Bulletin of Volcanology*, *56*(2), 98–107. https://doi.org/10.1007/BF00304105

Van Eaton, A., Herzog, M., Wilson, C., & Mcgregor, J. (2012). Ascent dynamics of large phreatomagmatic eruption clouds: The role of microphysics. *Journal of Geophysical Research (Solid Earth)*, *117*, 3203. https://doi.org/10.1029/2011JB008892

Witham, F., Blundy, J., Kohn, S. C., Lesne, P., Dixon, J., Churakov, S. V., & Botcharnikov, R. (2012). SolEx: A model for mixed COHSCl-volatile solubilities and exsolved gas compositions in basalt. *Computers & Geosciences*, *45*, 87–97. https://doi.org/10.1016/j.cageo.2011.09.021

Woods, A. W., & Wohletz, K. (1991). Dimensions and dynamics of co-ignimbrite eruption columns. *Nature*, *350*(6315), 225–227. https://doi.org/10.1038/350225a0

Zhang, Y., & Behrens, H. (2000). H2O diffusion in rhyolitic melts and glasses. *Chemical Geology*, *169*(1), 243–262. https://doi.org/10.1016/S0009-2541(99)00231-4

Zhang, Y., Xu, Z., Zhu, M., & Wang, H. (2007). Silicate melt properties and volcanic eruptions: SILICATE MELT PROPERTIES. *Reviews of Geophysics*, *45*(4). https://doi.org/10.1029/2006RG000216

759 Zhang, Y., Ni, H., & Chen, Y. (2010). Diffusion Data in Silicate Melts. *Reviews in Mineralogy and*

760 *Geochemistry*, *72*(1), 311–408. https://doi.org/10.2138/rmg.2010.72.8

761

762

Figure caption

Figure 1 *: Flow chart showing the calculation steps used in EMBER to determine the parameters and associated errors resulting in the best fit of natural volatile diffusion profiles. The outputs are a decompression rate and an initial (dissolved) volatile concentration as well as their associated confidence interval. This process of calculation is repeated for each value of exsolved volatile content (M_0). Estimation of the M_0 value and its related uncertainty is done in a similar manner but by considering the range of M_0 variation as the 4^{th} dimension of the starting matrix.*

Figure 2*: A display example of EMBER's GUI after a cycle of calculations. Input parameters are entered on the left panel (part 1) and results are displayed on the right (part 2). The input section is divided in three main parts, the grid search definition (1a), the main parameters and model selection (1b), and the parameters for the Monte-Carlo simulation (uncertainty and number of iterations) (1c). The result section is in three parts: comparison between best fit and natural diffusion profiles (2a), the result parameter of each best fit (2b) and the log section to follow the evolution of the calculation (2c). Clicking on the "Display all figures" once the program is done with the calculation will display best fits for each exsolved volatile content value and for each studied volatile specie. It also displays 3 3D-plots, of the evolution of the calculative error for each volatile(1) vs. the decompression rate and initial concentration, (2) the evolution of the decompression rate vs. exsolved volatile content and initial volatile concentration for each studied volatile specie and (3) the evolution of the cumulative error vs. decompression rate and exsolved volatile content (Figure 3).*

Figure 3*: Subset of plots generated from a calculation on the 1500CE Kīlauea reticulite ReaE1 studied previously by Ferguson et al., [2016]. (a) Influence of exsolved volatile content M_0 on best fit diffusion profiles of H_2O. Initial parameters from the grid search are listed in the caption. (b) Best fit diffusion profiles calculated by considering H_2O only (solid line) or all studied species (dashed lines). (c) Evolution of the cumulated scaled log_{10} (NErr_m) values over a range of decompression rate and exsolved volatile content. (d) Evolution of the NErr_m value for each volatile over a range of decompression rate and initial volatile content. The NErr_m values are in a log_{10}scale. The values of interest, linked to the smallest error value, are highlighted by a blue, red or yellow dot for H_2O, CO_2 and S respectively (d), and a black dot for the cumulative error (c).*

Figure 4 *: Comparison between recalculated data with EMBER and previous estimation from the literature. EMBER estimations are comparable with literature estimates with a few systematic differences (see text for details). Dashed line indicates the 1:1 ratio and thin solid lines indicates 2:1 and 0.5:1 ratios. Results from EMBER were acquired taking the input conditions of the respective original studies. Calculations for samples from Lloyd et al., :[2014] were made using their original H_2O diffusion coefficient. All the results displayed are*

calculated for M_0=0 excepted when original studies provided a range of M_0 [Ferguson et al., 2016]. *EMBER calculations were made using the "weighting and scaling of error" option which is a source of difference with previously reported literature decompression rate.*

Figure 5 : *Statistical repartition of all filtered decompression rate values with increasing iteration count of the Monte Carlo approach. The repartition gradually acquires a more pronounced shape. The red bars indicates the 1-σ confidence interval of those decompression rates while the blue, green and black ones respectively indicate the best-fit result, the median and the mean. Calculation is done with fixed initial concentration and exsolved volatile content. All displayed data are in MPa/s*

Figure 6*: Evolution of modeled relative decompression rates from H_2O (a), CO_2 (b) and S (c) as a function of the exsolved volatile content for a selection of embayments. Each case in a), b) or c) is calculated with a fixed P_{end}, reported in Table 2. For figures (d), (e) and (f), P_{ref} is the P_{end} value displayed in Table 2 for ReE2 and BT251. (d) The initial exsolved volatile content needed to generate the best fit ($M_{Bestfit}$) increases for ReE2 when changing Pend but not systematically for M413. (e) Variation of relative decompression rate modeled from the H_2O diffusion profile only with P_{end}. (f) Variation of relative decompression rate modeled from all studied species (H_2O, CO_2 and S for ReE2, and H_2O and CO_2 for M413) with P_{end}.*

Figure 7 *: (a) Compilation of EMBER-recalculated decompression rate as a function of eruption magnitude. The bigger mark indicates the highest decompression rate estimate for each eruption. For basaltic magmas, there is a trend of increasing decompression rate related to increasing magnitude only when considering the maximum decompression rate values. The trend does not apply to rhyolitic magmas. (b) Compilation of EMBER-recalculated decompression rate as a function of eruption plume height. The bigger mark indicates the highest decompression rate estimate for each eruption. With the exception of Ambrym, which plume maximal height is unknown and assessed by lava fountain height, there is a notable correlation between maximal decompression rate and plume height for basaltic magmas. The same caption applies for both figures. Magnitude estimates were calculated from either orginal article or respectively Shreve et al., [2019], Johnston et al., [2014], Self, [2006] and Mason et al., [2004] for Ambrym's 2018 eruption, Santorini's Minoan eruption, Taupo's Oruanui eruption and both Long Valley's Bishop Tuff and Yellowstone's Huckleberry Ridge Tuff. Plume height estimation comes from modelisations from Gardner et al., [1991], Mastin et al., [2014] and Van Eaton et al., [2012] respectively for Long Valley's Bishop Tuff, Yellowstone's Huckleberry Ridge Tuff and Taupo's Oruanui eruptions.*

Table caption

Table 1 : *Comparison of previously published codes. EMBER is a fully available complete software that covers a large spectrum of magma composition: dPdt = decompression rate, C_i = initial concentration, M_0 = exsolved volatile content, P_f = pressure of quench, gs stands for "grid search". Every study that model decompression rates from CO_2 and/or S uses the diffusion coefficients calculated from [Zhang et al., 2007]. The only two exceptions are the CO_2 diffusivity from [Liu et al.,*

2007] which is calculated from [Behrens and Zhang, 2001] and the S diffusivity from [Ferguson et al., 2016], which is calculated from [Freda et al., 2005].

***Table 2** : Re-calculated decompression rates with initial conditions and related eruption parameters. Ascent rates were calculated with density values from each original studies using the equation* $Asc\_rate = (Decomp\_rate/9.81 * Crustal\_density)$ 10^6 *with Decomp_rate in MPa/s, Asc_rate in m/s and the crustal density in kg/m3*

Tables

Table 1

Article	*Architecture*	*Volatiles studied*	*Magmatic composition*	*H_2O diffusion coefficient*	*Input parameters*	*M_0 study*	*Availability*
Liu et al, 2007	FORTRAN 77	H_2O	Rhyolitic	a	dPdt, C_i, T, M_0, P_f, P_0 *	yes	On request
Humphreys et al, 2008	COMSOL	H_2O	Rhyolitic	a ; b	dPdt, C_i P_f, P_0, T *		
Lloyd et al, 2014	n.d	H_2O,CO_2,S	Intermediate	Self-determined empiric law	dPdt, P_f, P_0, C_i, T *		
Ferguson et al, 2016	MATLAB	H_2O,CO_2,S	Basaltic	c	gs(dPdt, C_i, M_0), P_f, P_0, T	yes	
Myers et al, 2018	MATLAB	H_2O,CO_2	Rhyolitic	a	gs(dPdt, P_f, M_0), C_i, P_0, T	yes	On request
Moussallam et al, 2019	RStudio	H_2O	Basaltic	Constant (e)	dPdt, C_i, P_f, P_0, T	yes	Publicly Available
Newcombe et al, 2020	MATLAB	H_2O,CO_2,S	Intermediate	d	dPdt, M_0, P_f , P_0, T *	yes	
EMBER (This study)	MATLAB	H_2O,CO_2,S	Basaltic, Intermediate and Rhyolitic	e ; d ; a	gs(dPdt, C_i, M_0), P_f, P_0, T	yes	Publicly Available

a = [Zhang and Behrens, 2000]
b = [Nowak and Behrens, 1997]
c = [Zhang et al., 2010]
d = [Ni and Zhang, 2018]
e = [Freda et al., 2003]
*unconfirmed use of a grid search

Table 2

	Decompression rate (Mpa/s)				Ascent rate (m/s)	Initial concentration			M (wt%)	Time of ascension (s)	Pstart (MPa)	Pend (MPa)	T(°C)	Magnitude
	H2O based	CO2 based	S based	all species		H2O (wt%)	CO2 (ppm)	S (ppm)						
Ferguson et al., 2016														
IkiE1	0.03 +0.01 -0.00	0.02 +0.00 -0.00	0.04 +0.01 -0.00	**0.04 +0.00 -0.00**	1.4	0.60 +0.00 -0.00	300 +0 -0	1390 +0 -0	0.1 +0.1 -0.0	2755	107	0.1	1192	1.5
ReticE1	0.08 +0.03 -0.01	0.09 +0.02 -0.01	0.08 +0.04 -0.02	**0.08 +0.02 -0.01**	2.9	0.55 +0.00 -0.00	184 +0 -0	1316 +0 -0	1.6 +0.0 -0.0	553	47	2.75	1163	2.5
ReticE2	0.07 +0.03 -0.01	0.03 +0.01 -0.00	0.40 +0.00 -0.03	**0.06 +0.02 -0.00**	2.1	0.57 +0.00 -0.00	170 +0 -0	1320 +0 -0	3.2 +0.0 -0.0	676	40	0.1	1163	2.5
KeaE1	0.28 +0.10 -0.05	0.11 +0.04 -0.01	0.35 +0.25 -0.16	**0.26 +0.05 -0.04**	9.3	0.52 +0.03 -0.00	265 +5 -0	1415 +5 -0	1.6 +0.0 -0.0	185	50	2	1160	2.6
Moussallam et al., 2019														
AO2	**0.46 +0.27 -0.18**				16.0	1.32 +0.00 -0.00			0.1 +0.1 -0.0	110	50	0.1	1150	3.3
AO13	**0.12 +0.03 -0.01**				4.2	1.15 +0.00 -0.00			1.6 +1.6 -1.4	253	30	0.1	1150	3.3
AO38	0.17 +0.05 -0.03		0.39 +0.01 -0.16	**0.19 +0.08 -0.07**	6.7	1.15 +0.00 -0.00		403 +0 -0	0.8 +0.8 -0.5	237	45	0.1	1150	3.3
Lloyd et al., 2014														
E1	0.24 +0.01 -0.04	0.03 +0.00 -0.00	0.01 +0.00 -0.00	**0.06 +0.03 -0.02**	2.2	4.00 +0.00 -0.00	100 +0 -0	1500 +0 -0	0.1 +0.3 -0.1	3333	202	2	1030	4.4
E2	1.07 +0.29 -0.26	0.10 +0.00 -0.00	0.13 +0.34 -0.03	**0.30 +0.03 -0.09**	11.1	2.20 +0.10 -0.00	150 +3 -0	1900 +33 -0	0 +0.2 -0.0	175	54.6	2	1030	4.4
E3	0.92 +0.47 -0.21	1.47 +0.03 -0.59		**1.10 +0.32 -0.29**	40.9	2.80 +0.00 -0.00	160 +0 -0		1.6 +1.6 -1.2	69	78	2	1030	4.4
E4	0.35 +0.08 -0.05	0.28 +0.13 -0.08	0.46 +0.01 -0.27	**0.44 +0.01 -0.10**	16.3	2.80 +0.00 -0.00	170 +0 -0	2070 +0 -0	0.1 +0.1 -0.0	498	221	2	1030	4.4
Myers et al., 2018														
BTF7-1_RE_no_2	**0.021 +0.002 -0.003**				0.8	3.70 +0.10 -0.05			0.4 +2.8 -0.2	3238	78	10	740	8.5
BT_F2-5_RE_no_1	**0.041 +0.011 -0.010**				1.6	3.80 +0.00 -0.00			1.6 +1.6 -1.4	1014	77	35	740	8.5
BTF8-2_RE_no_1	**0.273 +0.061 -0.061**				10.7	5.00 +0.00 -0.00			0.1 +1.5 -0.1	264	131	59	740	8.5
P1963-6_RE_no_1	0.007 +0.002 -0.002	0.0001 +0.0004 -0.000		**0.002 +0.002 -0.001**	0.1	1.80 +0.00 -0.00	90 +0 -0		0 +0.8 -0.0	3846	38	13	780	8
P2305-F_RE_no_1	**0.020 +0.018 -0.000**				0.8	3.40 +0.00 -0.10			3.2 +0.0 -0.3	900	68	50	780	8
P1970-A_RE_no_6	0.068 +0.058 -0.035	0.010 +0.004 -0.000		**0.033 +0.072 -0.019**	1.3	3.40 +0.10 -0.00	90 +10 -0		0.1 +0.7 -0.1	515	89	54	780	8
MM4_RE_no_12	0.009 +0.014 -0.004	0.001 +0.000 -0.000		**0.005 +0.000 -0.000**	0.2	2.00 +0.00 -0.00	390 +0 -0		0 +0.1 -0.0	4934	85	40	800	9
MM7_RE_no_10	0.099 +0.065 -0.058	0.007 +0.000 -0.000		**0.013 +0.006 -0.006**	0.5	2.50 +0.56 -0.00	170 +8 -0		3.2 +0.0 -0.2	467	71	25	800	9
MM4_RE_no_13	0.069 +0.045 -0.018	0.152 +0.086 -0.080		**0.105 +0.081 -0.047**	4.1	2.80 +0.00 -0.00	290 +0 -0		1.6 +1.6 -1.4	1272	98	10	800	9
Humphreys et al., 2008														
KV518b-1	**0.16 +0.00 -0.00**				6.4	4.60 +1.66 -0.00			0	662	137	33	880	4.9
MSH1-3	**0.23 +0.00 -0.00**				9.3	6.50 +0.00 -0.52			0	481	137	27	880	4.9
MSH1-6	**0.82 +0.04 -0.02**				33.3	6.50 +0.00 -0.48			0	157	137	9	880	4.9
Moussallam et al. (2021)														
AF2	2.64 +1.55 -1.27		5.87 +0.14 -2.96	**2.64 +2.41 -1.55**	99.5	1.48 +0.03 -0.03		220 +10 -10	3.2 +0.0 -0.4	26	68	0.1	1110	4
AD5	0.49 +0.12 -0.08		0.14 +0.96 -0.04	**0.53 +0.19 -0.14**	19.9	1.05 +0.05 -0.10		950 +50 -100	0.1 +0.3 -0.1	64	34	0.1	1110	4
AE38	0.11 +0.03 -0.02		0.01 +0.00 -0.00	**0.11 +0.04 -0.03**	4.2	1.05 +0.10 -0.00		950 +233 -0	0 +0.2 -0.0	335	37	0.1	1110	4
PG11	1.70 +0.87 -0.59		0.10 +0.06 -0.00	**1.70 +0.86 -0.59**	64.1	1.80 +0.20 -0.10		797 +33 -17	1.6 +1.6 -1.4	68	115	0.1	1110	4
Myers et al, 2021														
18R1F	**1.70 +0.86 -0.75**				66.7	4.70 +0.10 -0.00			0	49	143	60	850	7.4
18R1O	**1.70 +0.56 -0.40**				66.7	4.30 +0.08 -0.00			0	55	119	26	850	7.4
18R2O	**0.43 +0.05 -0.05**				16.9	4.60 +0.00 -0.00			0	274	120	2	850	7.4
20R1O	**0.47 +0.01 -0.08**				18.4	3.35 +0.05 -0.03			0	153	77	5	850	7.4
11R6O	**2.93 +1.32 -1.31**				114.8	4.30 +0.10 -0.00			0	26	116	40	850	7.4

Figure 1.

STEP 1

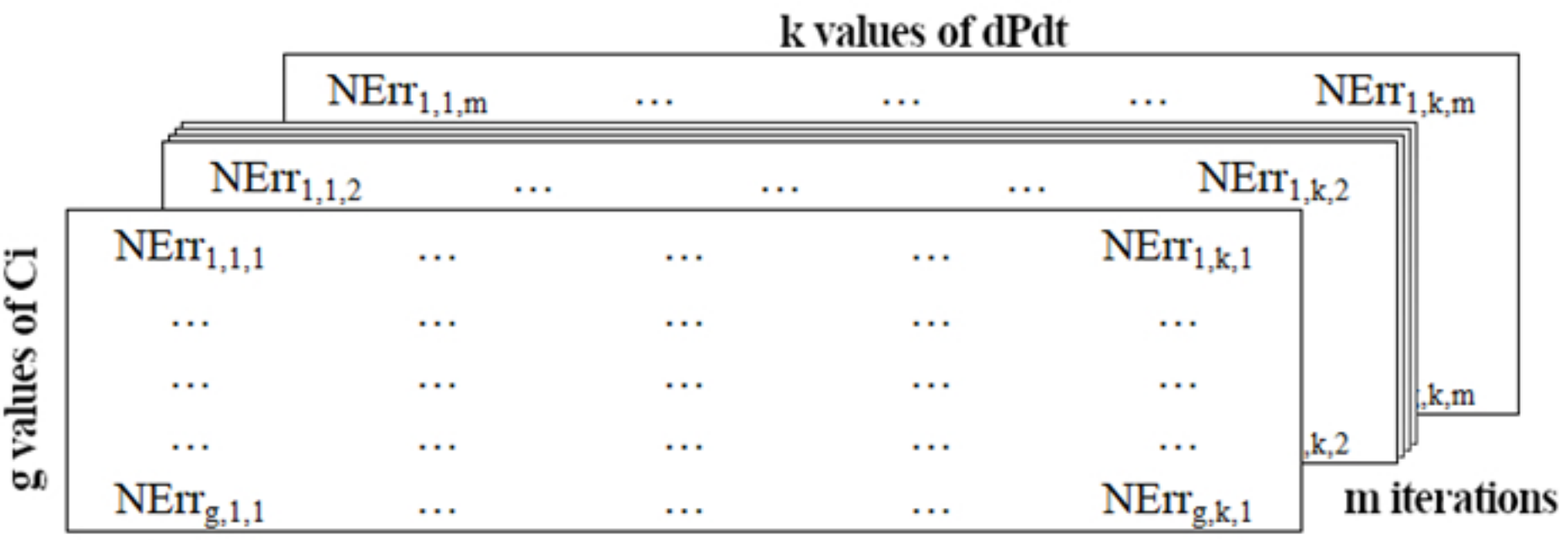

-Mean for each $NErr_{ij}$ values over the m iterations

-Select the minimal NErr_m value

-Calculation of 1 sigma confidence interval over the $NErr\_m_{a,b}$ value

STEP 2

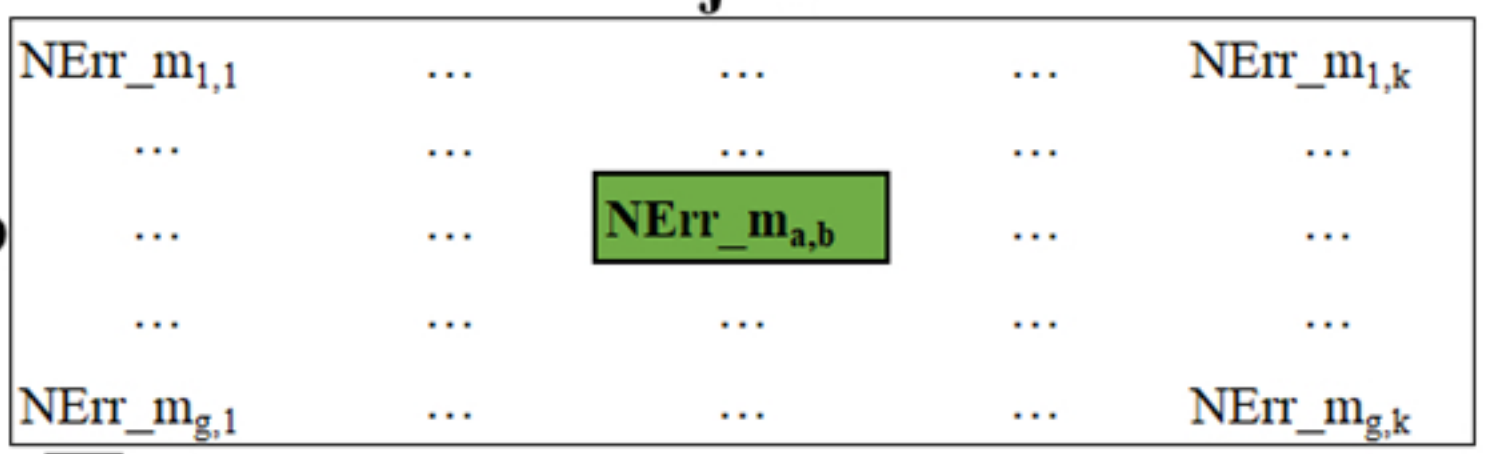

-Filtering of error values using equation 10

STEP 3

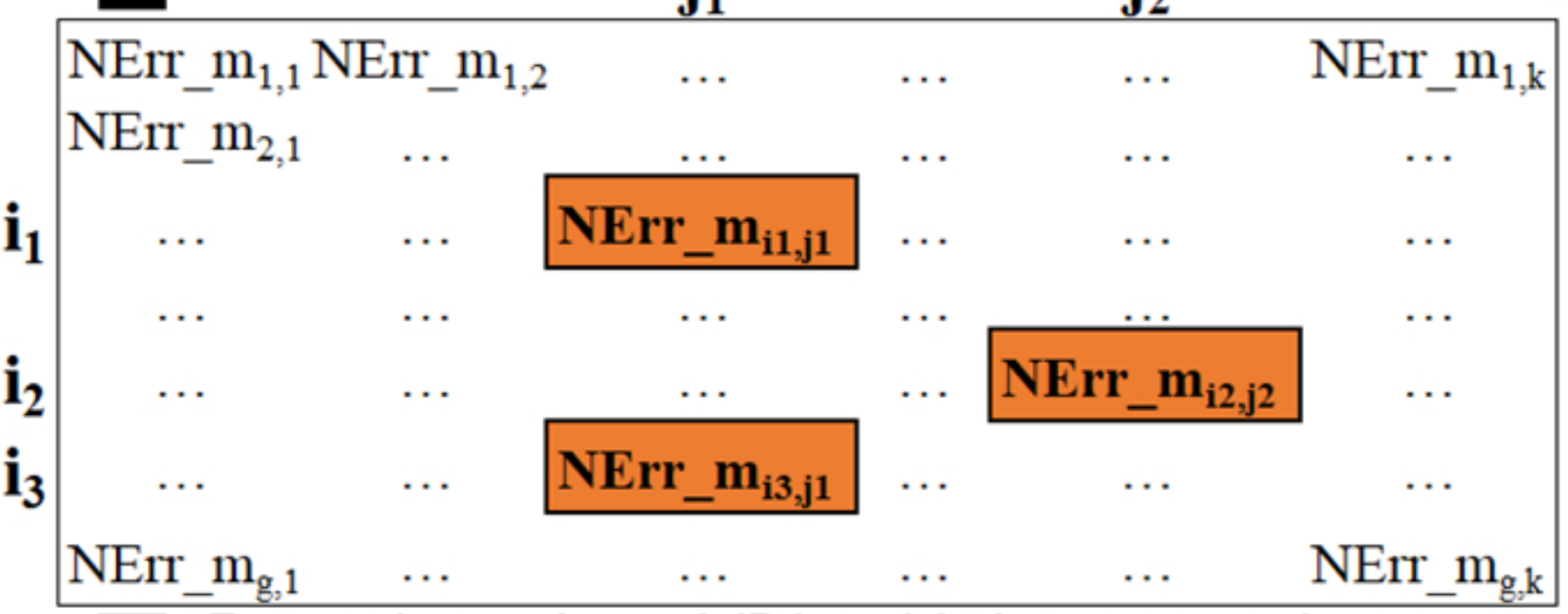

-Extract the n values of dPdt and C_i that were used to calculate all the filtered $NErr\_m_{i,j}$

STEP 4

from all j	from all i
$dPdt_1$	C_{i1}
…	…
$dPdt_n$	C_{in}

STEP 5

-Result value of C_i and dPdt

-1 sigma confidence interval of C_i and dPdt

Smallest value among the whole matrix with (a,b) as its coordinates

All $NErr\_m_{i,j}$ values that satisfy equation 10

Figure 2.

Part 1: Inputs

Part 2: Results

EMBER

Grid Search

1a

	Min	Max	Step
dPdt (MPa/s)	0.02	0.4	30
Cinit H2O (wt%)	0.57	0.63	4
Cinit CO2 (ppm)	170	192.5	
Cinit S (ppm)	1320	1330	

M value (wt%) (space separated) :

0 0.1 0.2 0.4 0.8 1.6 3.2

General Inputs

1b

Temperature (°C): 1163

Pstart (MPa): 40

Pend (MPa): 2.75

File type:
- (•) Solex
- ( ) VolatileCalc

Magma Chemistry:
- Rhyolitic
- Intermediate
- Basaltic

☑ CO2 study ☑ S study

Set working directory

Uncertainty parameters

1c

H2O 2RSD (%)	6
CO2 2RSD (%)	4
S 2RSD (%)	2
Variability of spot place (µm)	2

Mole fraction of Si: 0.5

Molar mass of anhydrous melt: 35.5

Number of iterations: 101

Name of the embayment: ReE2

☑ Weighting and scaling of error

Compute

Calculation done

Best profiles

2a

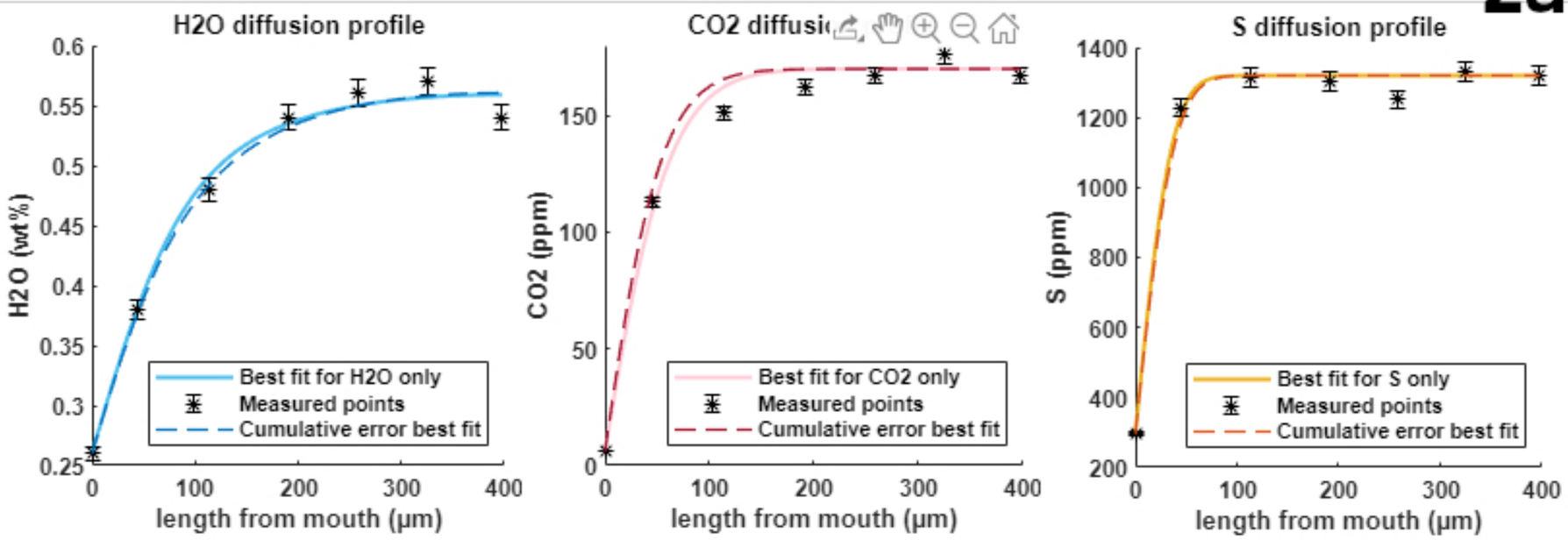

Results

2b

Name	DecompRate (MPa/s)	1 Std_Dev (MPa/s)	Ascent time (s)	Initial volatile concentration (wt% or ppm)	Least error
ReE2					
M= 0 wt%					
H2O	0.02	0 +0.013103	2000	0.57	204.7775
CO2	0.046207	0 +0.013103	865.6716	170	29.6565
S	0.072414	-0.013103 +0.026207	552.381	1320	51.4625
M= 0.1 wt%					
H2O	0.02	0 +0	2000	0.59	74.5534
CO2	0.046207	0 +0.013103	865.6716	170	29.223
S	0.072414	-0.013103 +0.032103	552.381	1320	57.8211
M= 0.2 wt%					
H2O	0.02	0 +0	2000	0.61	40.8031
CO2	0.046207	0 +0.013103	865.6716	170	26.5181
S	0.072414	-0.013103 +0.026207	552.381	1320	53.0929
M= 0.4 wt%					
H2O	0.02	0 +0.019655	2000	0.63	79.8492
CO2	0.046207	0 +0.013103	865.6716	170	27.0156
S	0.072414	-0.013103 +0.026207	552.381	1320	62.6618

Log:

2c

Finding the best fit for all volatiles
Saving files and figures
Calculation done in :1 hours, 44 minutes and 34 seconds
Calculation fully terminated

EMBer v 1.0

Last updated : 01-Apr-2021

Display all figures

Figure 3.

a

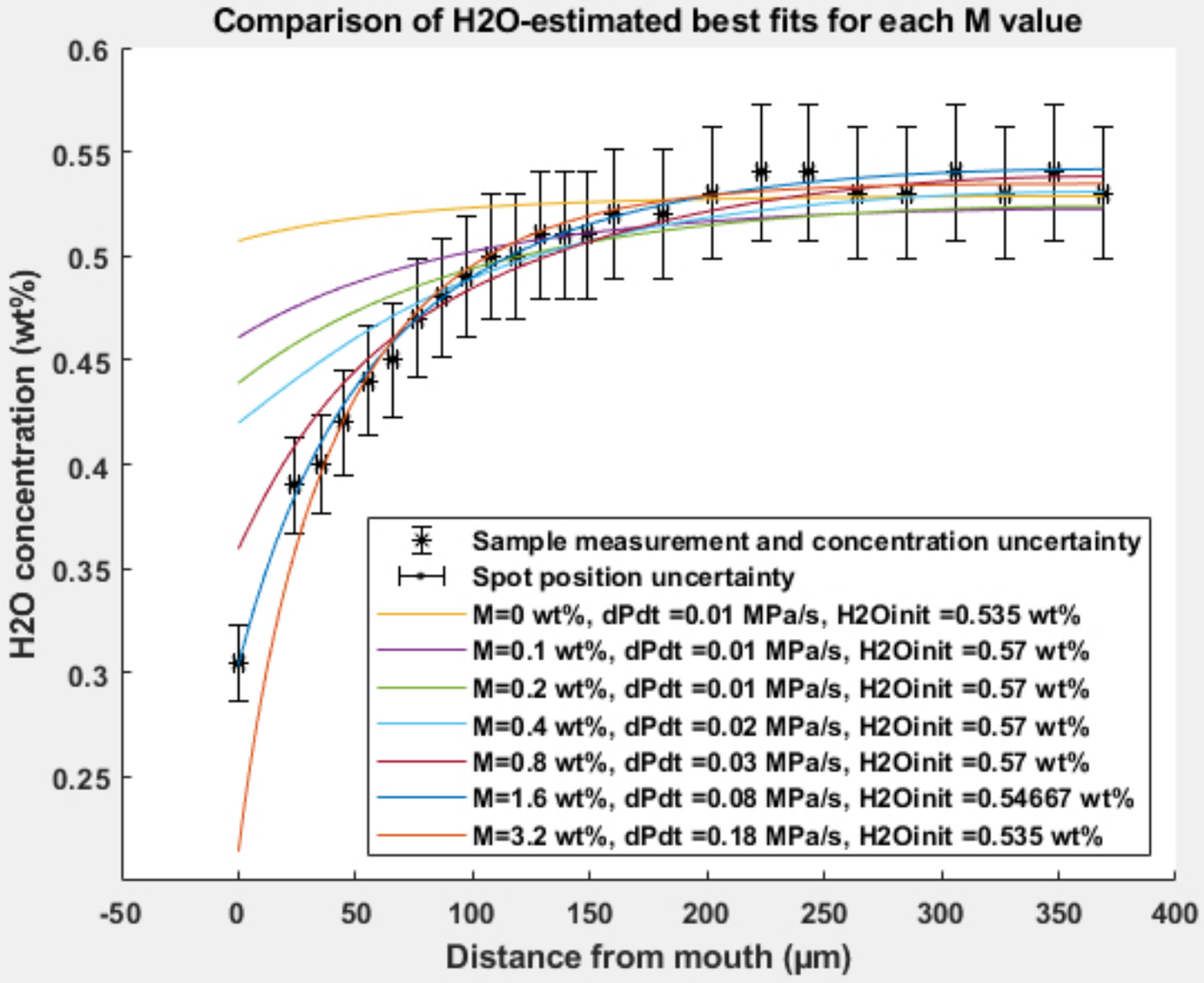
Comparison of H2O-estimated best fits for each M value
H2O concentration (wt%)
Distance from mouth (µm)
Sample measurement and concentration uncertainty
Spot position uncertainty
M=0 wt%, dPdt =0.01 MPa/s, H2Oinit =0.535 wt%
M=0.1 wt%, dPdt =0.01 MPa/s, H2Oinit =0.57 wt%
M=0.2 wt%, dPdt =0.01 MPa/s, H2Oinit =0.57 wt%
M=0.4 wt%, dPdt =0.02 MPa/s, H2Oinit =0.57 wt%
M=0.8 wt%, dPdt =0.03 MPa/s, H2Oinit =0.57 wt%
M=1.6 wt%, dPdt =0.08 MPa/s, H2Oinit =0.54667 wt%
M=3.2 wt%, dPdt =0.18 MPa/s, H2Oinit =0.535 wt%

b

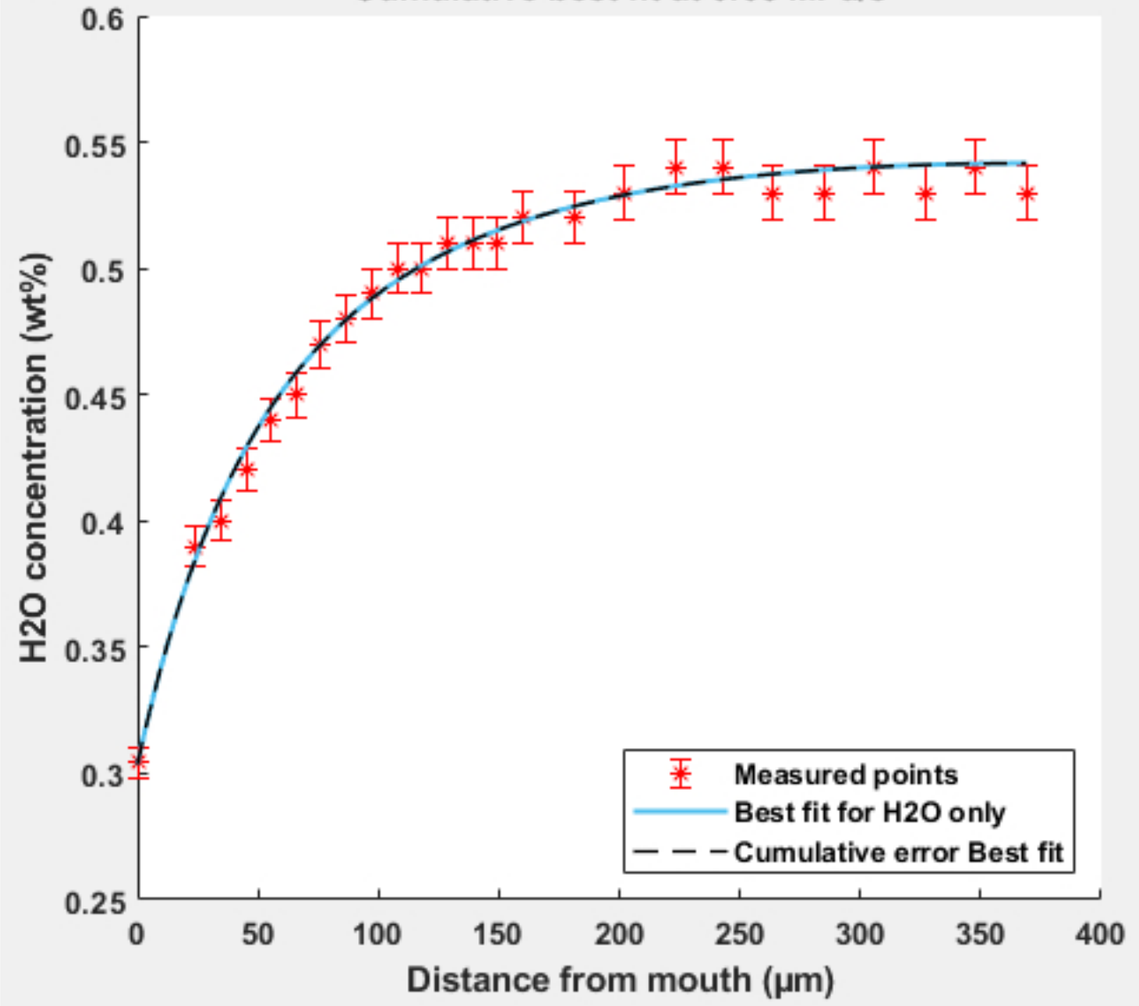
Cumulative best fit at 0.08 MPa/s
H2O concentration (wt%)
Distance from mouth (µm)
Measured points
Best fit for H2O only
Cumulative error Best fit

C

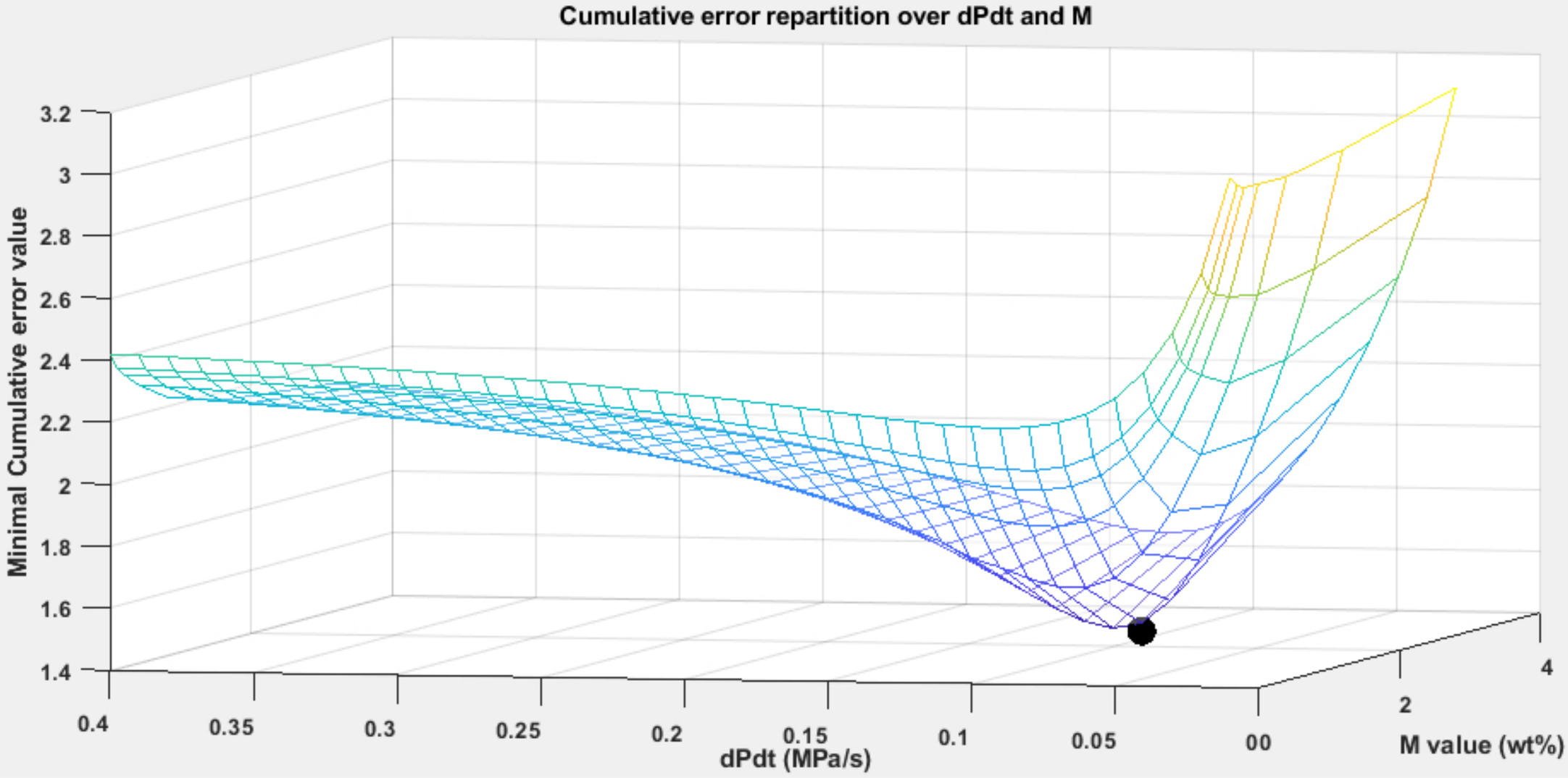
Cumulative error repartition over dPdt and M
Minimal Cumulative error value
dPdt (MPa/s)
M value (wt%)

d

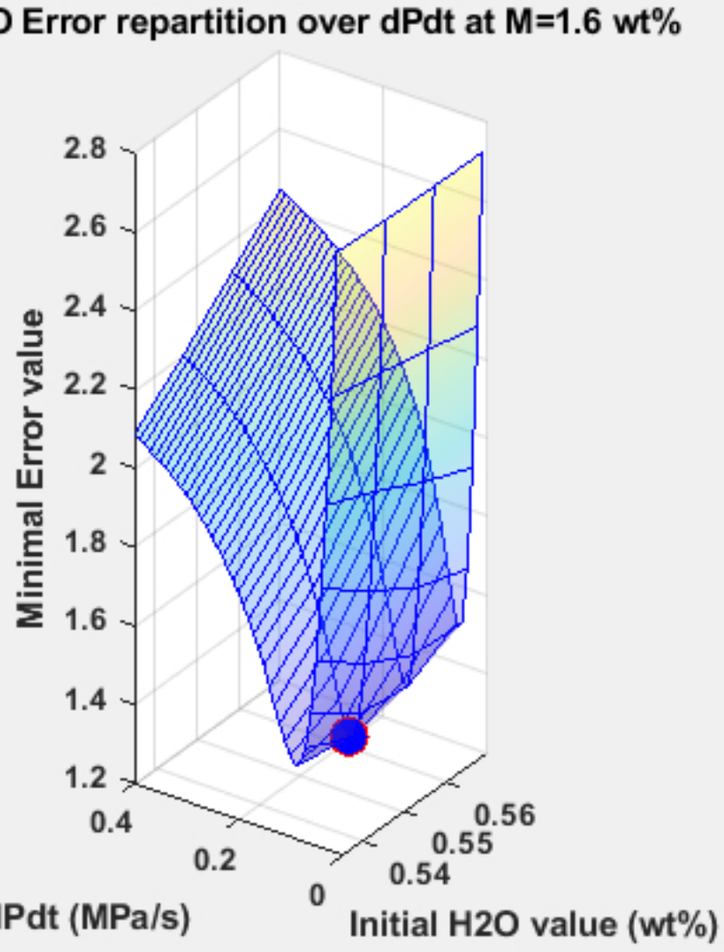
H2O Error repartition over dPdt at M=1.6 wt%
Minimal Error value
dPdt (MPa/s)
Initial H2O value (wt%)

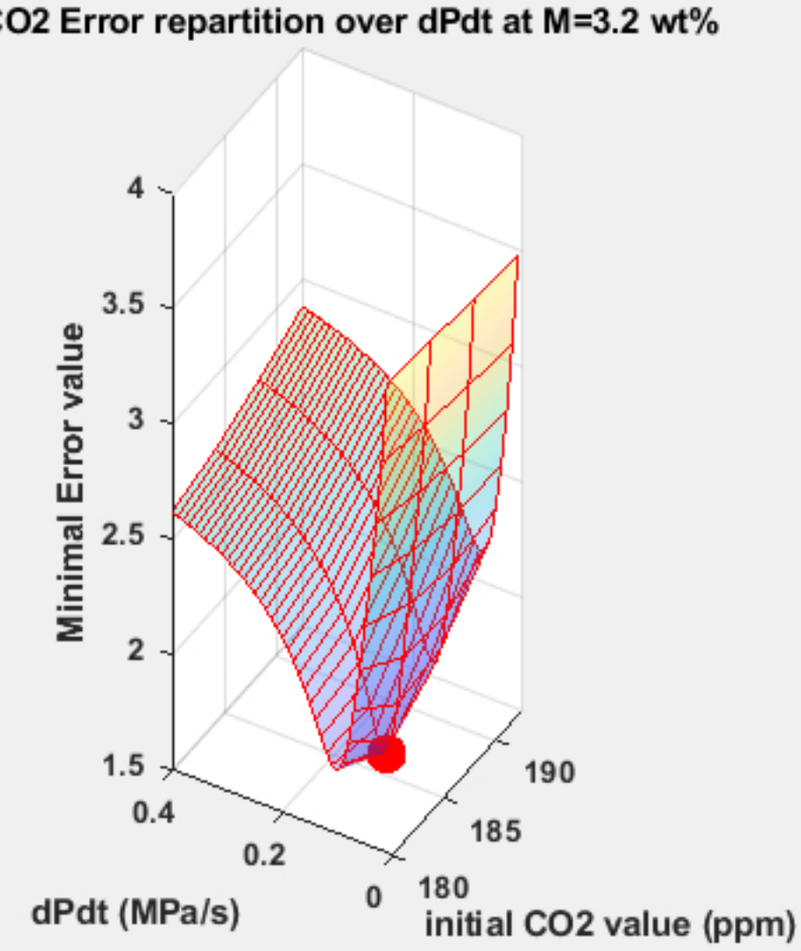
CO2 Error repartition over dPdt at M=3.2 wt%
Minimal Error value
dPdt (MPa/s)
initial CO2 value (ppm)

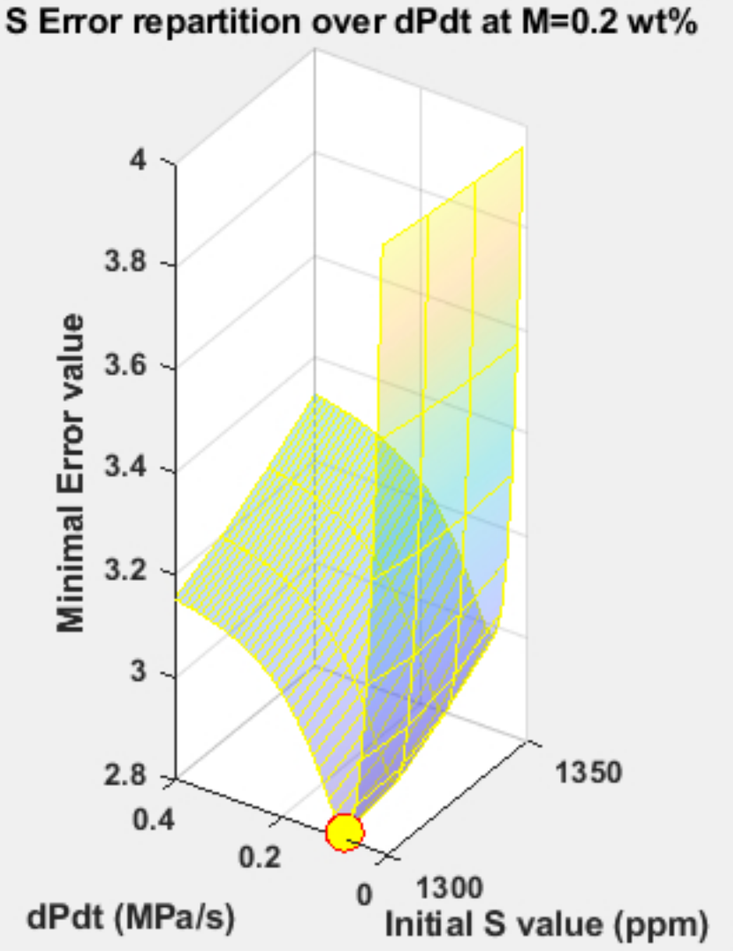
S Error repartition over dPdt at M=0.2 wt%
Minimal Error value
dPdt (MPa/s)
Initial S value (ppm)

Figure 4.

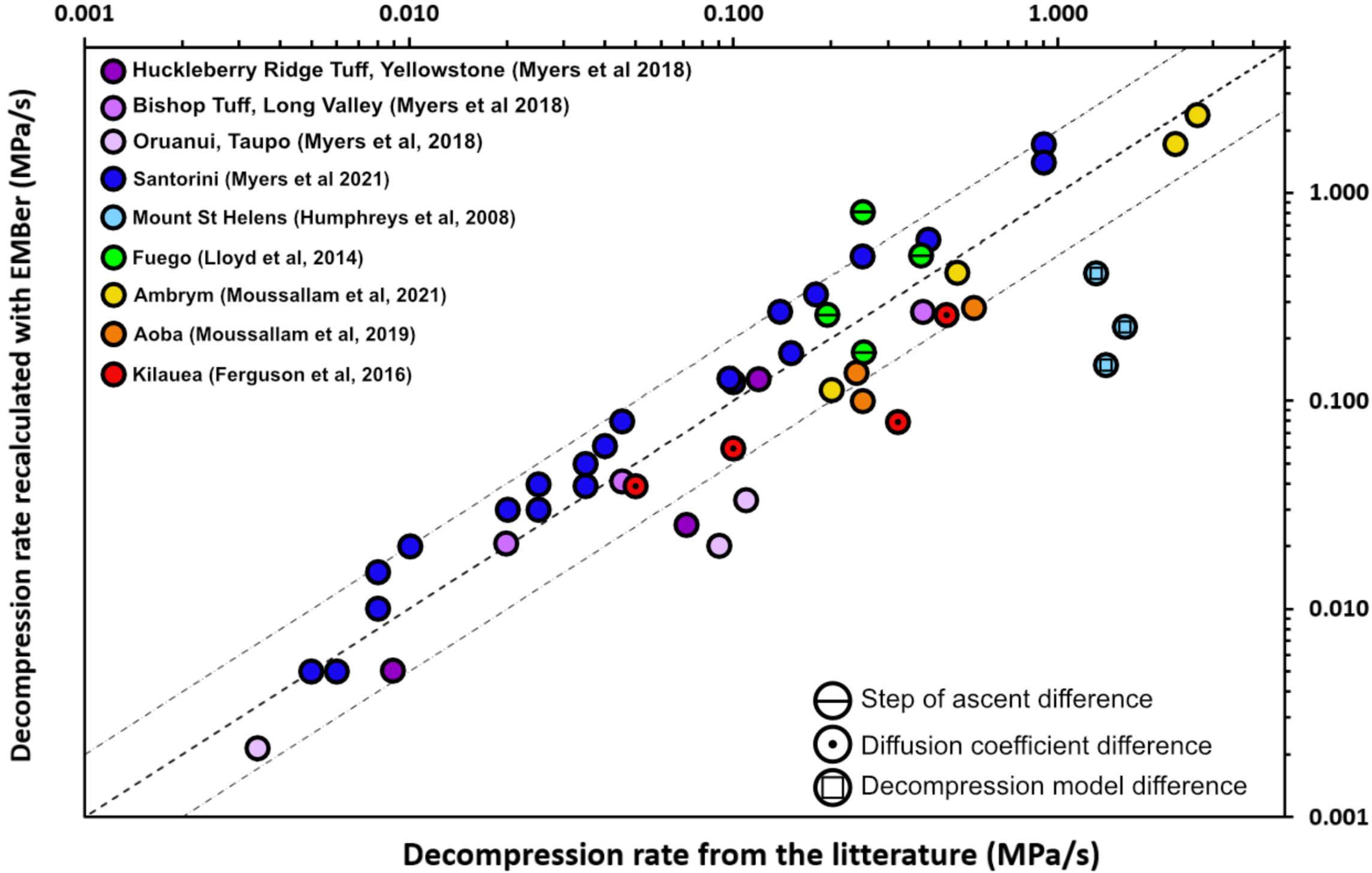
0.001
0.010
0.100
1.000
Huckleberry Ridge Tuff, Yellowstone (Myers et al 2018)
Bishop Tuff, Long Valley (Myers et al 2018)
Oruanui, Taupo (Myers et al, 2018)
Santorini (Myers et al 2021)
Mount St Helens (Humphreys et al, 2008)
Fuego (Lloyd et al, 2014)
Ambrym (Moussallam et al, 2021)
Aoba (Moussallam et al, 2019)
Kilauea (Ferguson et al, 2016)
Step of ascent difference
Diffusion coefficient difference
Decompression model difference
Decompression rate recalculated with EMBer (MPa/s)
Decompression rate from the litterature (MPa/s)

Figure 5.

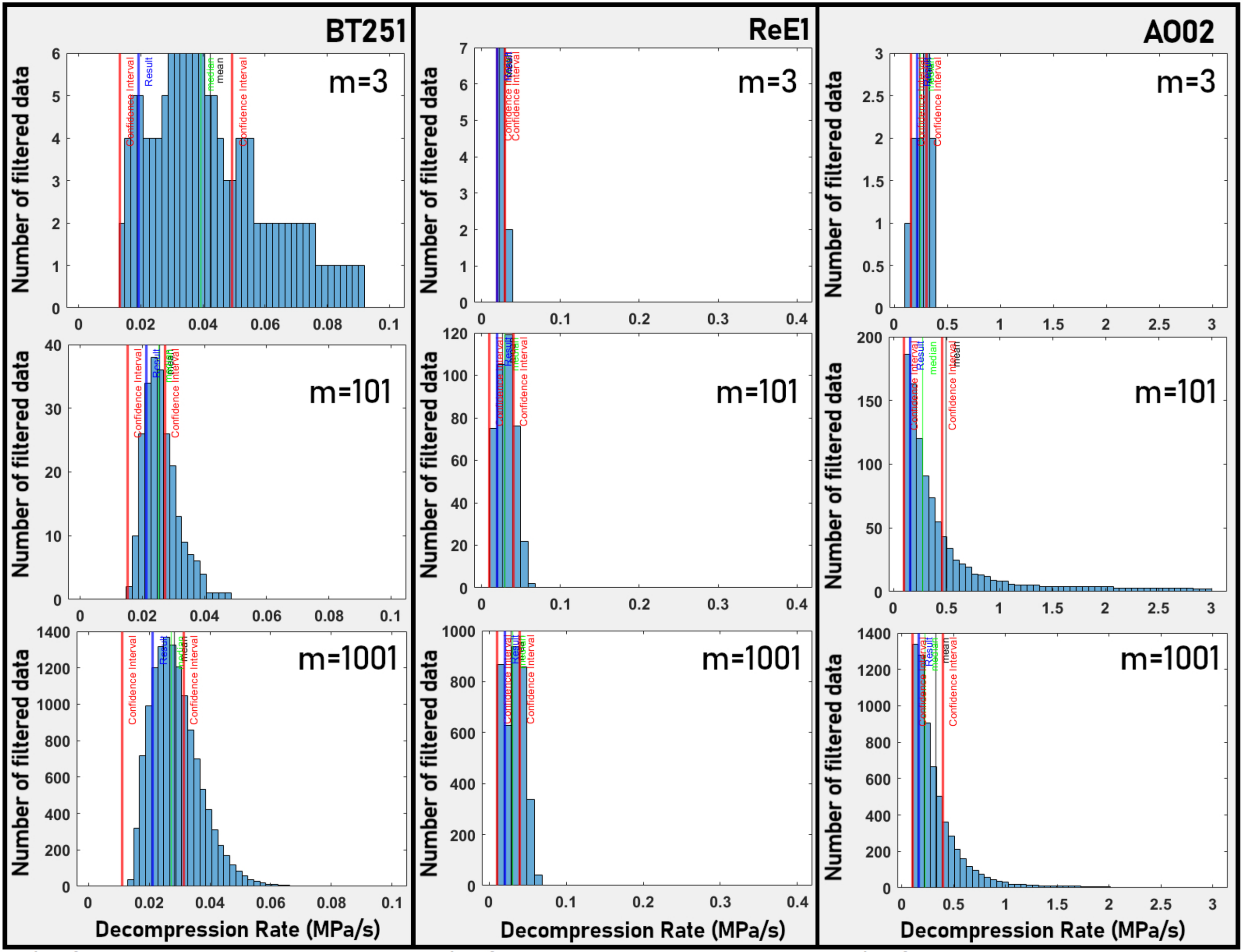

number of iterations	3	11	101	501	1001
BT251					
Result	0.019	0.021	0.021	0.021	0.021
Median	0.039	0.023	0.025	0.027	0.027
Mean	0.042	0.022	0.026	0.027	0.028
Uncertainty	-0.006	-0.004	-0.006	-0.008	-0.01
	+0.03	+0.004	+0.006	+0.008	+0.01

number of iterations	3	11	101	501	1001
ReE1					
Result	0.020	0.020	0.020	0.020	0.020
Median	0.020	0.020	0.030	0.020	0.030
Mean	0.022	0.023	0.027	0.023	0.028
Uncertainty	-0	-0	-0.01	-0	-0.01
	+0.01	+0.02	+0.02	+0.03	+0.02

number of iterations	3	11	101	501	1001
AO02					
Result	0.218	0.218	0.159	0.159	0.159
Mean	0.248	0.218	0.278	0.218	0.218
Median	0.236	0.250	0.498	0.287	0.326
Uncertainty	-0.059	-0.059	-0.059	-0.059	-0.059
	+0.089	+0.202	+0.296	+0.178	+0.237

Figure 6.

M_0 study

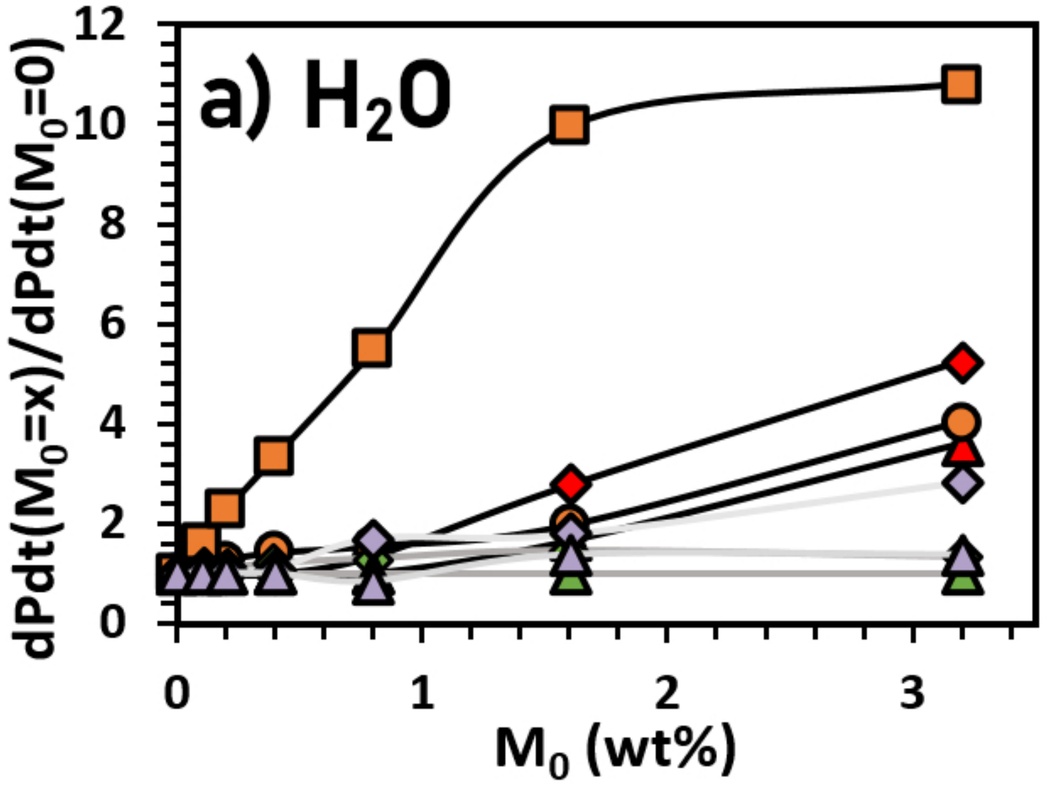

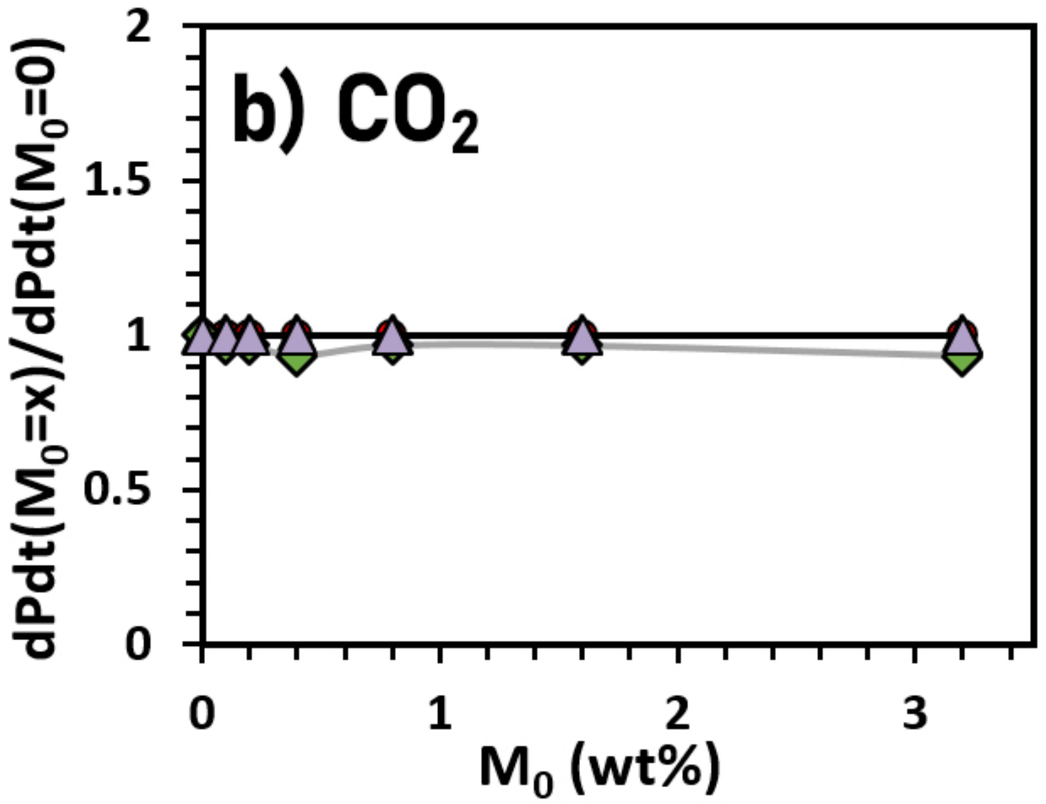

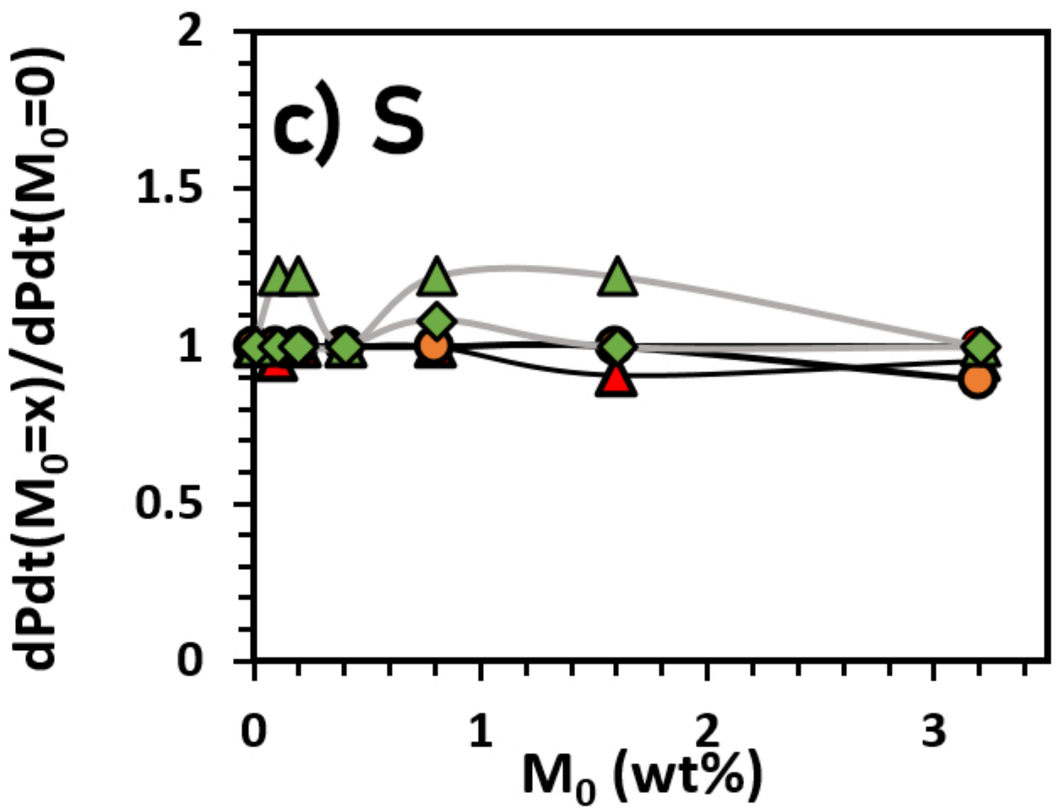

P_{end} study

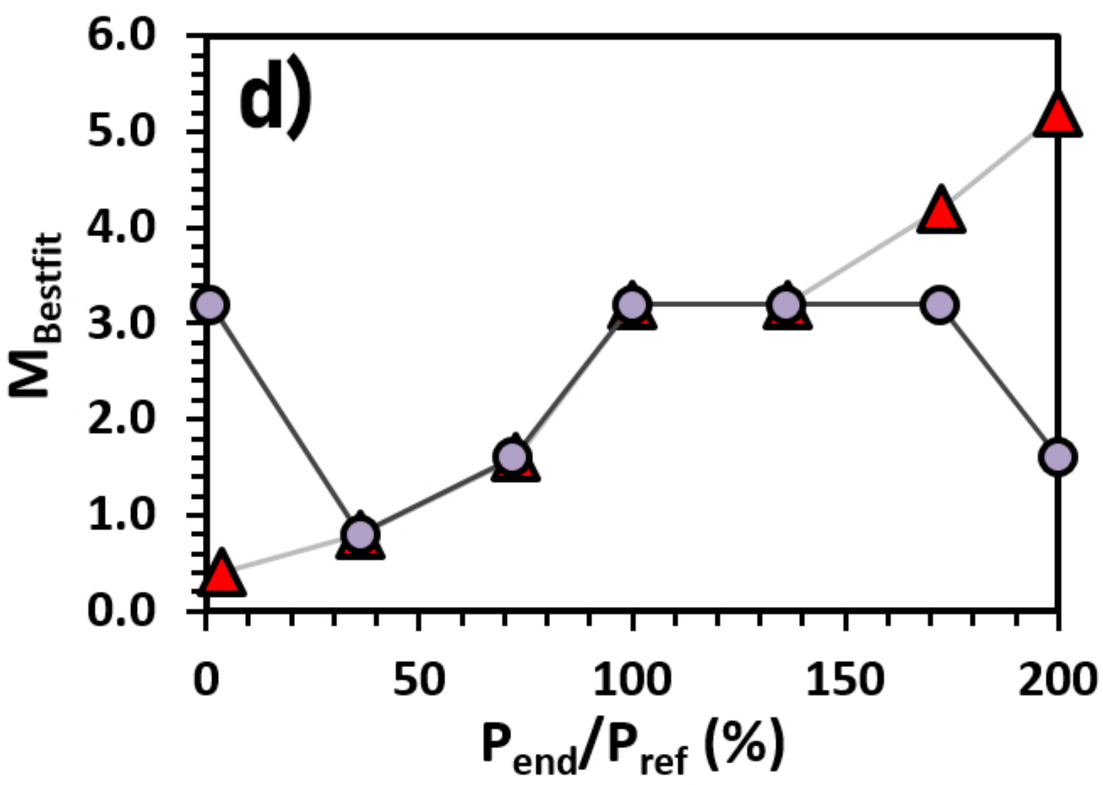

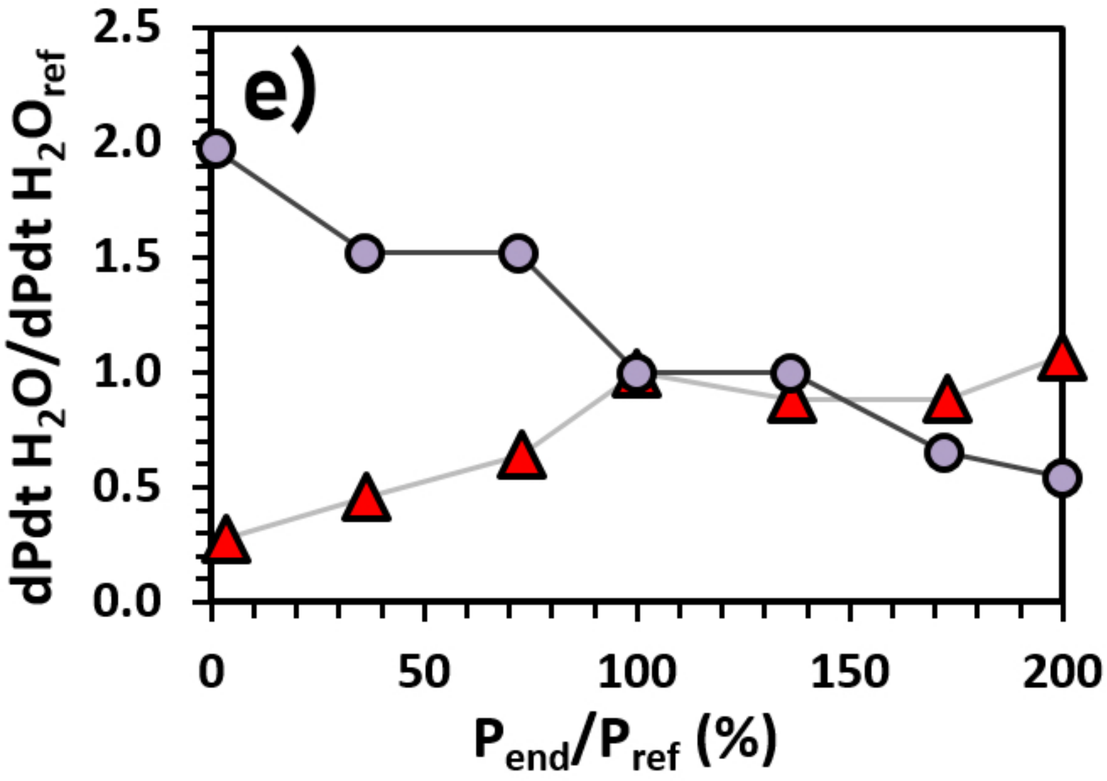

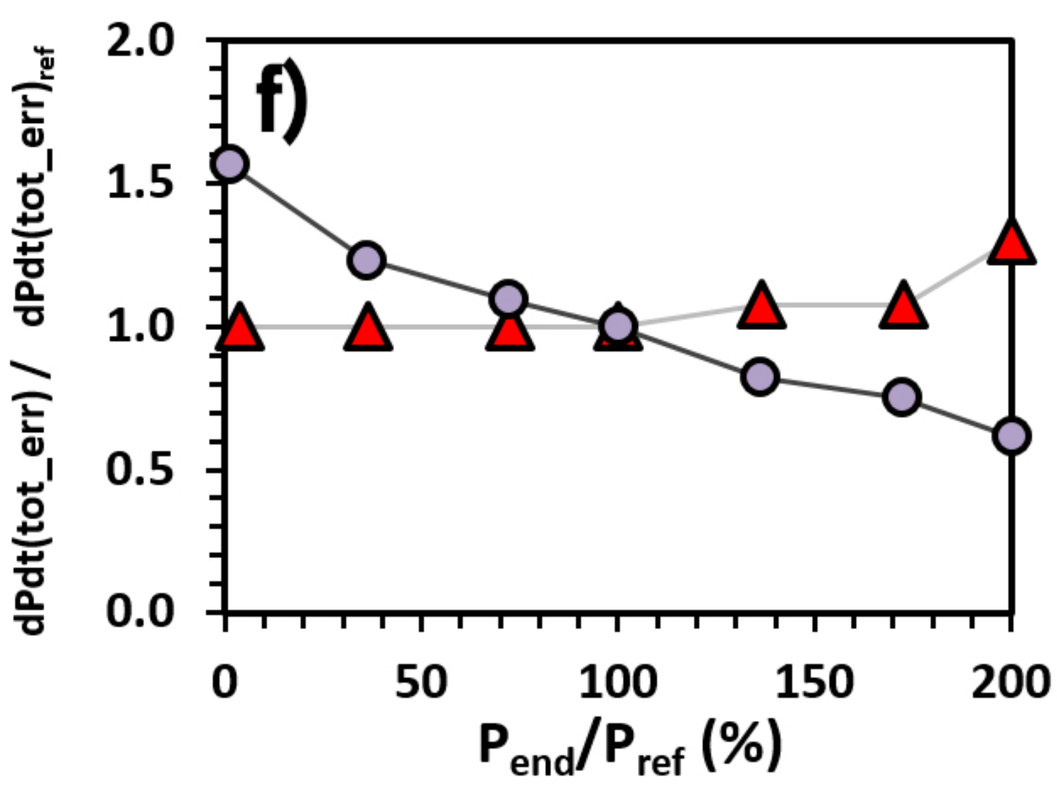

KeE1
ReE2
AO38
AO02
E2
E4
P636
BT821
M413

Figure 7.

a)

Mafic Compositions

Silicic Compositions

Basaltic trend

Ambrym 2018
Basaltic, Hawaiian

Fuego 1974
Basaltic-Andesitic, Sub-Plinian

Mt St Helens 1980
Silicic, Plinian

Ambae 2017-2018
Basaltic, Plinian

Kilauea 1650, Hawaii
Basaltic, Sub-Plinian

Kilauea 1500, Hawaii
Basaltic, Hawaiian

Kilauea 1959, Hawaii
Basaltic, Hawaiian

Santorini Minoan eruption
Silicic, Ultra-Plinian

Long Valley 0.767Ma
Bishop Tuff Silicic

Yellowstone 2.08Ma
Huckleberry Ridge Tuff
Silicic

Taupo 25.4ka Oruanui
Silicic

Decompression rate recalculated with EMBER (MPa/s)

10.00
1.00
0.10
0.01

0 1 2 3 4 5 6 7 8 9 10

Eruption magnitude

(Ferguson et al, 2016)
(Moussallam et al, 2019)
(Moussallam et al, 2021)
(Lloyd et al, 2014)
(Humphreys et al, 2008)
(Myers et al 2021)
(Myers et al 2018)

b)

Highest decompression rate recalculated with EMBER (MPa/s)

10.00
1.00
0.10
0.01

0.01 0.1 1 10 100

Plume Height (km)